The Institute for Solid State Physics
The University of Tokyo
5-1-5 Kashiwanoha, Kashiwa, Chiba 277-8581
http://www.issp.u-tokyo.ac.jp

Activity Report: The Institute for Solid State Physics (ISSP) The University of Tokyo 2008

The Institute for Solid State Physics
The University of Tokyo

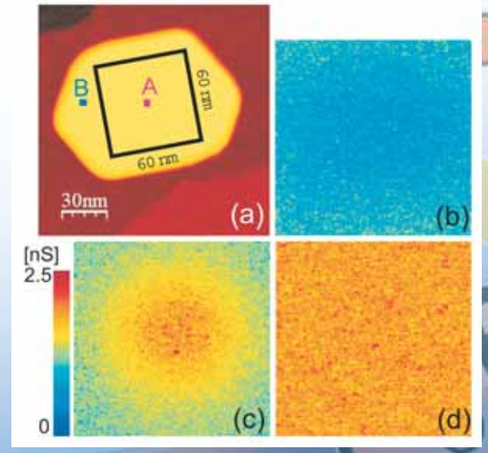

Activity Report 2008

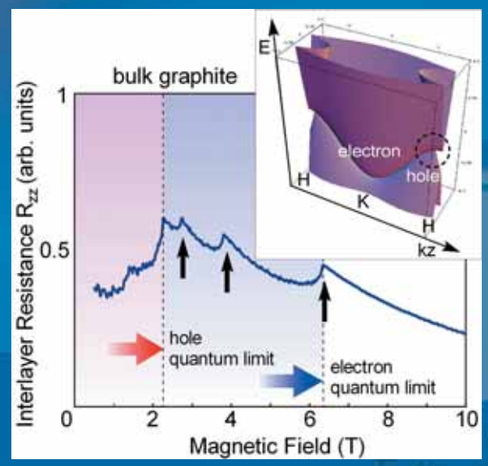

ISSP

Activity Report 2008

Contents

Preface

This booklet constitutes the annual report of the activity of the Institute for Solid State Physics (ISSP) of the University of Tokyo for the fiscal year 2008.

ISSP was established in 1957 as a joint-use central research institution in the field of basic materials science. After its 40 years of operation at the Roppongi campus, ISSP relocated itself to a new campus in Kashiwa city and started afresh in April 2000. In 2005, ISSP underwent an external evaluation by an international review committee. In the review, evaluation was given on the research accomplishments, especially those utilizing new facilities installed at the time of relocation. The scientific achievements during the first 5 years of research activity in Kashiwa were highly praised. Valuable comments and suggestions were also given on the future research directions and the betterment of the ISSP management. In November 2007, ISSP celebrated its 50th anniversary and held a commemorative symposium at the former Roppongi campus, which has been renovated as the National Art Center and the National Graduate Institute for Policy Studies.

ISSP is thus moving forward in the second 50 years with its mission as a hub of the basic materials science research in Japan. In addition to the various on-going researches summarized in this booklet, there are several important projects whose status range from actual construction stage to planning/ budget-seeking stage. The long-pulse high magnetic field laboratory shall offer a versatile platform for experiments in high magnetic field. Together with the short-pulse megagauss field installation already in operation, it constitutes the International MegaGauss Science Laboratory. A new synchrotron radiation beam-line at the SPring-8 facility shall be in operation in autumn this year and a new neutron beam-line is under construction at the J-PARC MLF facility. Other projects vigorously promoted in collaboration with the respective communities include, an advanced coherent light laboratory envisaged as a state-of-the-art facility of ultrafast, short-wavelength and high-peak-power lasers, and a computational materials science project planned in conjunction with the Next-Generation Supercomputer.

June, 2009

Yasuhiro Iye
Director
Institute for Solid State Physics
The University of Tokyo

Research Highlights

Phase Diagram and Spin Dynamics in Volborthite with a distorted Kagomé Lattice

Takigawa and Hiroi Groups

The search for exotic ground states in two-dimensional (2D) spin systems with frustrated interactions is a challenge in condensed matter physics. In particular, the spin-1/2 antiferromagnetic Heisenberg model on a kagomé lattice, a 2D network of corner-sharing equilateral triangles, is believed to have spin-liquid ground state with no broken symmetry. All candidate materials known to date, however, depart from the ideal kagomé model in one way or another due to disorder, structural distortion, anisotropy, or longer range interactions. Vorlborthite $Cu_3V_2O_7(OH)_2{\cdot}2H_2O$ is an example, which, unlike the ideal model, has kagomé-like layers formed by isosceles triangles. Consequently, it has two Cu sites and two kinds of exchange interactions (Fig. 1, inset). Nevertheless, the absence of magnetic order down to 2 K, much lower than the Curie-Weiss temperature 115 K, indicates strong effects of frustration [1]. Recently, Yoshida *et al.* have significantly improved sample quality by hyfrothermal annealing, allowing us to study intrinsic properties at lower temperatures [2].

We have performed ^{51}V-NMR experiments on a high-quality powder sample of volborthite. The NMR spectrum at B = 1 T shows a sudden broadening near T = 1 K (Fig. 2) accompanied with a sharp peak in the nuclear spin-lattice relaxation rate $1/T_1$ (Fig. 3), indicating a

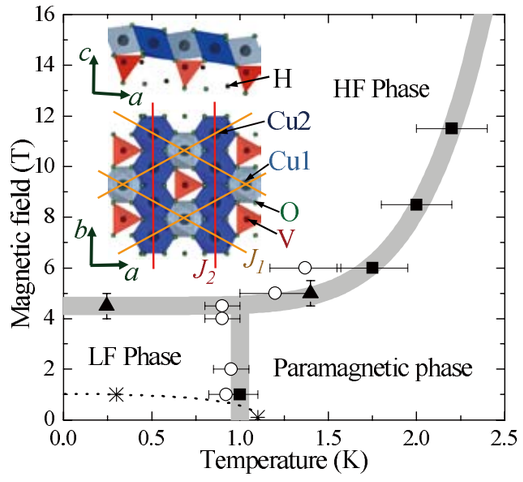

Fig. 1. (Inset) The crystal structure of $Cu_3V_2O_7(OH)_2{\cdot}2H_2O$. (main panel) The phase diagram proposed by the present study. The squares (triangles) represent the phase boundaries determined from the NMR spectra as function of temperature (Fig. 2) (magnetic field). The circles and asterisks indicate the peak of $1/T_1$ (Fig. 3) and the onset of the hysteresis in the susceptibility [2].

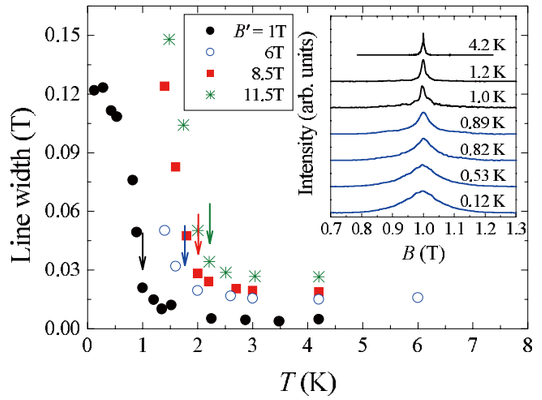

Fig. 2. T-dependence of the line width (FWHM) at various magnetic fields. (B' stands for the center of gravity of the spectrum.) The inset shows the NMR spectra at 11.243 MHz (B'=1 T).

magnetic transition. Similar but weaker anomalies have been reported previously [3], which coincided with the hysteresis of the susceptibility. Since the hysteresis in our sample is suppressed below 0.3 K at 1 T, the magnetic transition has nothing to do with the spin-glass like behavior. The dynamics in the low temperature phase is quite unusual. The T-linear behavior of $1/T_1$ (Fig. 3) below 0.6 K indicates highly enhanced low-energy fluctuations incompatible with the spin-wave theory. The spin-echo decay rate $1/T_2$ also shows anomalous enhancement and reaches a finite value at T = 0, indicating extremely slow fluctuations. This means the power spectrum of the local spin correlation $G(t) = \langle \boldsymbol{S}(t){\cdot}\boldsymbol{S}(0)\rangle$ has at least two frequency scales as illustrated in Fig. 3. Although line broadening and a peak in $1/T_1$ are normally considered evidence for a magnetic order, it

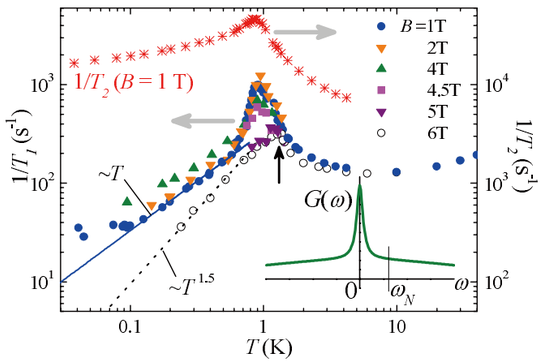

Fig. 3. T-dependence of $1/T_1$ at various magnetic fields B. The asterisks represent the T-dependence of $1/T_2$ at 1 T. The solid (dotted) line shows the power law dependence T^{α} with α = 1 (1.5). The inset shows a schematic illustration of $G(\omega)$, the power spectrum of the local spin correlation function, with two distinct frequency scales.

remains still open in our case whether the order is truly static in the sense that $G(t)$ remains finite in the limit of $t \to \infty$.

We found a sudden change of the NMR spectra when the field exceeds 4.5 T, where the first magnetization step was observed [2]. The behavior of $1/T_1$ also changes qualitatively (Fig. 3), indicating a second magnetic phase with distinct spin structure and dynamics at high B. The B-T phase diagram established by our work is shown in Fig. 1. We expect more phases will be identified by future work.

References
[1] Z. Hiroi, N. Kobayashi, M. Hanawa, M. Nohara, H. Takagi, Y. Kato, and M. Takigawa, J. Phys. Soc. Jpn. **70**, 3377 (2001).
[2] H. Yoshida, Y. Okamoto, T. Tayama, T. Sakakibara, M. Yokunaga, A. Matsuo, Y. Narumi, K. Kindo, M. Yoshida, M. Takigawa, and Z. Hiroi, J. Phys. Soc. Jpn. **78**, 043704 (2009).
[3] F. Bert, D. Bono, P. Mendels, F. Ladieu, F. Duc, J.-C.Trombe, and P. Millet, Phys. Rev. Lett. **95**, 087203 (2005).

Authors
M. Yoshida, M. Takigawa, H. Yoshida, Y. Okamoto, and Z. Hiroi

Antiferromagnetism in AFe_2As_2 (A=Ba, Sr): the Parent Compounds of the New Iron Pnictide Superconductors

Takigawa and Ohgushi Groups

The discovery of high temperature superconductivity in the layered iron-pnictide compounds, first in RFeAsO$_{1-x}$F$_x$ (R: La or other rare earth elements) [1] and subsequently in $A_{1-x}B_x$Fe$_2$As$_2$ (A=Ba, Sr, Ca; B=K, Na), with the superconducting transition temperature exceeding 50 K has opened new opportunities to investigate the interplay between magnetism and superconductivity. The undoped parent compounds (RFeAsO and AFe_2As_2) are compensated metals and undergo an antiferromagnetic (AF) transition. The superconductivity appears upon elemental substitution or, in the case of AFe_2As_2, by applying pressure.

We have performed the nuclear magnetic resonance (NMR) experiments on ^{75}As nuclei using high quality single

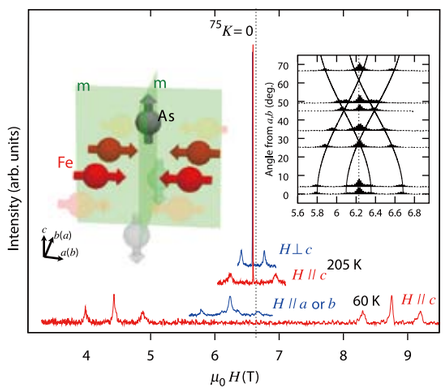

Fig. 1. ^{75}As-NMR spectra in $SrFe_2As_2$ at 48.31 MHz obtained by sweeping the magnetic field along the c-axis (red) or along the a- or b- axis (blue). A single set of quadrupole-split three lines is observed in the paramagnetic state (205 K). Below T_t = 199K symmetric line splitting occurs for H // c, while the lines shift without splitting for $H \perp c$, indicating that the staggered fields due to AF order is parallel to the c-axis. This in turn determines the stripe-type spin structure shown in the left inset. The right inset shows the angular variation of the NMR spectra at T = 20 K with the field rotated in the ab-plane.

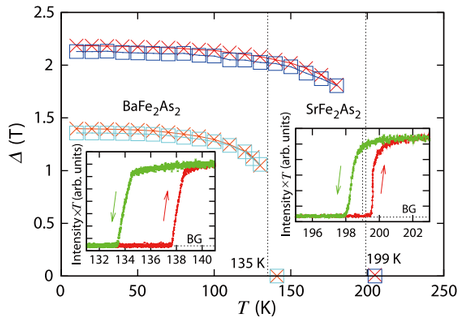

Fig. 2. T-dependence of the hyperfine field Δ due to AF order in $BaFe_2As_2$ and $SrFe_2As_2$. Δ is determined from the splitting of the central line for H // c (crosshairs) or from the line shift for $H \perp c$. The T-dependences of the intensity of the central line at the paramagnetic resonance fields shown in the insets provide clear evidence for the first order AF transitions with hysteresis.

crystals of $BaFe_2As_2$ and $SrFe_2As_2$. The NMR spectra shown in Fig. 1 split symmetrically upon entering into the AF phase for the field along the c-axis but not for the field along the a- or b- axis. This result combined with the symmetry of the hyperfine interaction between As nuclei and Fe moments imposed by the crystal structure allowed us to select uniquely the stripe-type AF spin structure shown in the left inset of Fig. 1. Evidence for the orthorhombic crystal distortion in the AF phase was provided by the two sets of quadrupole satellite lines. The splitting of each set shows identical angular variation in the ab-plane with a phase shift of 90 degrees (Fig. 1 right inset). Similar results were obtained also for $BaFe_2As_2$.

Figure 2 shows the T-dependence of the hyperfine field due to AF moments, which is proportional to the staggered moments. The discontinuous jump at the transition temperature indicates first order transitions for both materials. This is further confirmed by the hysteresis in the temperature dependence of the intensity of the central line at the paramagnetic resonance field (inset in Fig. 2).

Figure 3 shows the T-dependence of the nuclear spin-lattice relaxation rate divided by temperature $1/(T_1T)$. It shows substantial enhancement in the paramagnetic phase near the transition temperature, indicating development of the AF spin fluctuations. In particular, $BaFe_2As_2$ shows strong enhancement only for H // c. Such anisotropy may be due to orbital-selective spin fluctuations through the spin-orbit coupling. A finite value of $1/(T_1T)$ at low temperatures indicates that a part of the Fermi surface survives in the AF phase. Work is now in progress to investigate pressure induced superconductivity.

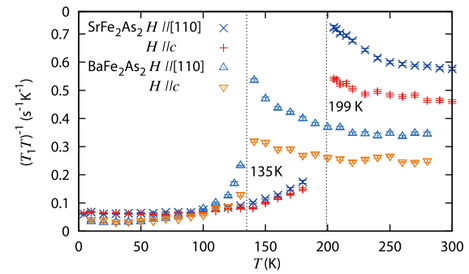

Fig. 3. T-dependence of the nuclear spin-lattice relaxation rate divided by temperature $(T_1T)^{-1}$ in $BaFe_2As_2$ and $SrFe_2As_2$ for different field orientations. In $BaFe_2As_2$ strong enhancement of $(T_1T)^{-1}$ near T_t is observed only for H // c, indicating development of anisotropic spin fluctuations at the stripe wave vector.

References
[1] Y. Kamihara, T. Watanabe, M. Hirano, and H. Hosono, J. Am. Chem. Soc. **130**, 3296 (2008).
[2] K. Kitagawa, N, Katayama, K. Ohgushi, M. Yoshida, and M. Takigawa, J. Phys. Soc. Jpn. **77**, 114709 (2008).
[3] K. Kitagawa, N, Katayama, K. Ohgushi, and M. Takigawa, J. Phys. Soc. Jpn. **78**, (2009) in press.

Authors
K. Kitagawa, N. Katayama, K. Ohgushi, M. Yoshida, and M. Takigawa

Low-Temperature Magnetization of a non-Kramers doublet ground state system $PrMg_3$: Evidence of the quadrupole Kondo effect

Sakakibara Group

In the cubic compound $PrMg_3$, the J = 4 multiplet of Pr^{3+} ($4f^2$) ion splits into four levels due to the crystalline electric field (CEF) effect, and the ground state becomes a Γ_3 non-Kramers doublet. Interestingly, this doublet has no magnetic dipole moment; it carries purely multipole (two electric quadrupoles and one magnetic octupole) degrees of freedom. Previous specific heat $C(T)$ measurements revealed no signature of a phase transition above 0.5 K [1]. How the degeneracy of the Γ_3 doublet is lifted as $T \rightarrow 0$ has been a matter of considerable interest. The reported C/T value reaches a huge value of about 2.8 J/mol K^2 at 0.54 K [1], suggesting a formation of a heavy fermion state arising from the purely multipole degrees of freedom.

Unfortunately, the crystal structure of $PrMg_3$ is of Heusler type in which a random site exchange between Pr and Mg atoms may occur. The site disorder locally breaks cubic symmetry around Pr sites, and would weakly split the Γ_3 doublet with an amplitude that may have some distribution. This effect causes a continuous releasing of the entropy of the doublet, resulting in a large low-T specific heat. Thus the specific heat data alone are not convincing to assert the heavy fermion state whose entropy releasing is due to quantum fluctuations. In order to explore evidence of the possible Kondo effect, we have performed magnetization

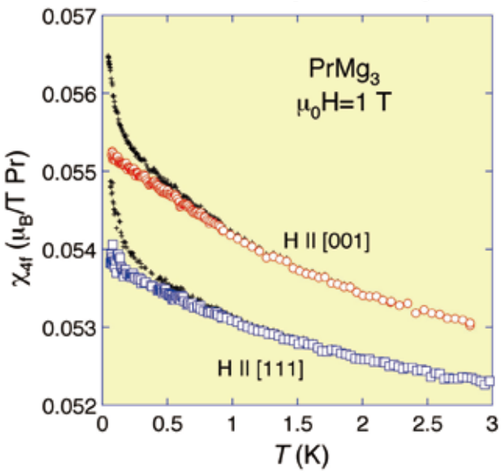

Fig.1 4f-electronic part of the magnetic susceptibility of $PrMg_3$ obtained in a field of 1 T. Crosses denote the raw data including the Pr nuclear contribution.

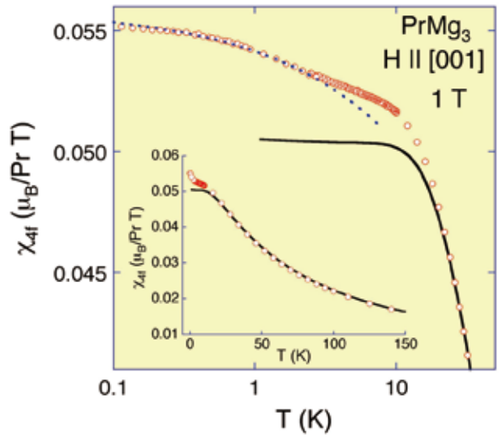

Fig. 2 Log-T plot of χ_{4f} below 30 K. The inset shows a linear plot up to 150 K. Solid lines represent the behavior expected from the CEF calculation. Dashed line shows a $-T^{1/2}$ dependence predicted for a quadrupole Kondo model.

measurements on a single crystal of $PrMg_3$ down to 60 mK in fields up to 8.5 T [2]. It can be shown that the magnetic susceptibility of the Γ_3 doublet system is much less affected by a site disorder than the specific heat.

Figure 1 shows the 4f electronic part of the susceptibility χ_{4f} obtained in a field of 1 T applied along [001] (circles) and [110] (squares) directions. Here the Pr nuclear Curie term is subtracted from the data. For both directions, a continuous increase in χ_{4f} is observed on cooling below 3 K. We found that this increase is not suppressed even in a strong field of 7 T, ruling out the effect of magnetic impurities.

Figure 2 shows $\chi_{4f}(T)$ in a wider temperature range. We found that $\chi_{4f}(T)$ below 10 K is significantly enhanced over the T-independent Van-Vleck behavior calculated for the CEF level scheme of the present system (solid lines), and continues to increase down to the lowest temperature. This anomalous behavior of $\chi_{4f}(T)$ is intrinsic to $PrMg_3$. We consider that the low-T enhancement of $\chi_{4f}(T)$ comes from hybridization between 4f and conduction electrons. The dotted line in Fig.2 is a $-T^{1/2}$ behavior theoretically predicted for the quadrupole Kondo effect in a Γ_3 doublet ground state system [3]. Our data well obey this $-T^{1/2}$ behavior in a temperature interval $0.3 < T < 2.5$ K. A deviation from the $-T^{1/2}$ dependence is observed in $\chi_{4f}(T)$ at very low temperatures below 0.3 K, which is reasonable since the theory is based on an impurity model whereas $PrMg_3$ is a lattice system. The present experimental results strongly support the occurrence of the quadrupole Kondo effect in $PrMg_3$.

References
[1] H. Tanida, H.S. Suzuki, S. Takagi, H. Onodera, and K. Tanigaki, J. Phys. Soc. Jpn. **75** 073705 (2006).
[2] T. Morie, T. Sakakibara, H.S. Suzuki, H. Tanida, and S. Takagi, J. Phys. Soc. Jpn. **78** 033705 (2009).
[3] D.L. Cox and M. Makivic: Physica B **199-200** 391 (1994).

Authors
T. Morie, T. Sakakibara, H.S. Suzuki[a], H. Tanida[b], and S. Takagi[b]
[a]National Institute for Material Science
[b]Tohoku University

Magnetic Torque Studies on d-π electron System $TPP[Fe(Pc)(CN)_2]_2$

Tajima Group

The title compound $TPP[Fe(Pc)(CN)_2]_2$ is a one-dimensional molecular conductor that exhibits giant negative magnetoresistance (GNMR) [1]. Here, Pc and TPP denote phthalocyanine and tetraphenylphosphonium, respectively. This GNMR is an interesting phenomenon, since it is not caused by a sharp transition such as the field-induced metal-insulator transition. It is highly anisotropic for the magnetic field direction, reflecting molecular orientation of $[Fe(Pc)(CN)_2]$.

Figure 1(a) shows the crystal structure of $TPP[Fe(Pc)(CN)_2]_2$. The Pc ring in $[Fe(Pc)(CN)_2]$ affords π electrons that form a conduction band in the solid state. The Fe(III) at the center of the ring is in the low-spin state with S = 1/2. Because of the four-fold symmetry of $[Fe(Pc)(CN)_2]$, orbital magnetic moment of Fe(III) is not completely quenched. Consequently, Fe(III) behaves as a local magnetic moment having highly anisotropic g factors (g_{xx} = 0.52, g_{yy} = 1.11, g_{zz} = 3.62) [2]. There are strong interactions between the π electrons in the Pc ring and the d electrons of Fe(III). This intra-molecular d-π interaction is the origin of the GNMR phenomena in molecular conductors of $[Fe(Pc)(CN)_2]$. In order to study this GNMR phenomena in detail, magnetic states of both d and π electron systems in $[Fe(Pc)(CN)_2]$ salts should be clarified on the basis of microscopic pictures. However, attempts to do so had not succeeded.

Recently we have measured the magnetic torque and heat capacity of $TPP[Fe(Pc)(CN)_2]_2$ salt and analyzed them together with magnetic susceptibility data [3]. Our study revealed that: i) the peak in the magnetic susceptibility data

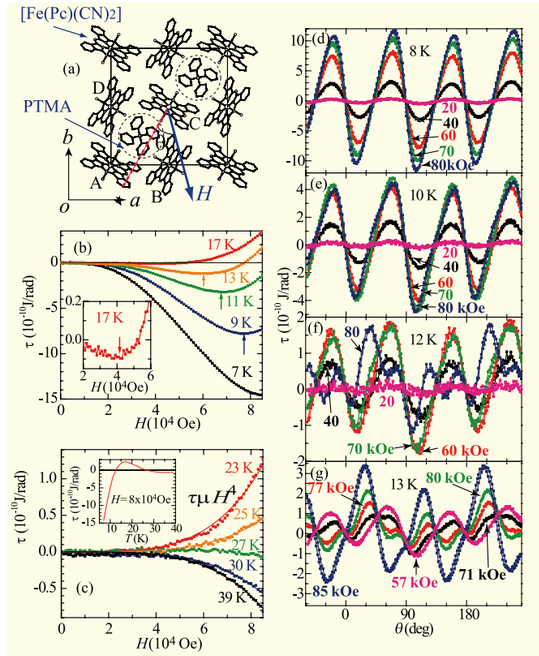

Fig. 1. (a) The definition of the field direction and crystal structure of $TPP[Fe(Pc)(CN)_2]_2$. (b),(c): Field dependence of the magnetic torque at θ = 22.5 deg. (d)-(g): Magnetic torque curves at 8, 10, 12, 13 K.

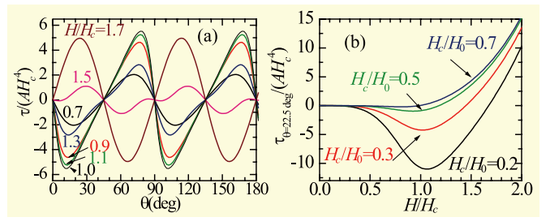

Fig. 2. (a) The simulation of the torque curves based on Eqs. (2) and (3) at H_c / H_0 = 0.3. (b) Field dependence of the torque amplitude calculated using Eqs. (2) and (3).

around 25 K is due to the antiferromagnetic short-range order of d-electrons; ii) π electrons fall into an antiferromagnetic state below 13 K, with fluctuations of state appearing even at 17 K; and iii) an anomalously large spin-flop field (80 kOe at 9 K) is observed for the π-electron antiferromagnetic state. In this paper we report the summary of our study.

Figures 1(b) & (c) show the field-strength dependence of the magnetic torque at θ = 22.5° below 17 K and above 23 K, respectively. The magnetic torque in the lowest field is negative below 17 K. As the field increases, the torque reaches a minimum and abruptly increases, finally becoming positive. In the temperature range above 23 K, the torque is almost proportional to H^4 on both the positive and negative sides. Inversion of the torque curve occurs around 27 K. Figures 1(d)~(g) show the toque curves measured at 8, 10 12, 13 K. Interestingly, very complicated torque curves appear at 12 and 13 K.

In order to analyze the results, we numerically calculated magnetic torque due to d electrons using the anisotropic Heisenberg model in one dimension. The calculation was performed in the range of H < 100 kOe and T > 10 K using the exchange interactions $J_{x,y}/k_B$ = 16 K and J_z/k_B = 32 K. Based on this calculation, we found the torque curves are approximated by the following equation:

$$\tau_d(H, \theta, T) = A(T)H^4 \sin(4\theta) \quad (1)$$

$A(T) > 0$ ($T \leq 30$ K); $A(T) < 0$ ($T \geq 30$ K)

This equation well explains the torque-curve inversion experimentally observed around T=27 K.

The complicated torque curves below 13 K cannot be explained in this model. In order to interpret them, we added the torque component of the antiferromagnetic π electrons in this way:

$$\tau(H, \theta) = \tau_d(H, \theta) + \{\tau_C(H, \theta) + \tau_D(H, \theta)\}/2. \quad (2)$$

Here, $\tau_C(H, \theta)$ and $\tau_D(H, \theta)$ respectively represent the torque component for the antiferromagnetic chains of π spins formed by molecules C and D (see Fig. 1a). This contribution is given by

$$\tau_D(H, \theta) = -\frac{\chi_\perp - \chi_{//}}{2} H^2 \sin\left\{\arctan\frac{\sin 2\theta_D}{\cos 2\theta_D - (H/H_c)^2}\right\}\cos\varphi_D, \quad (3)$$

where $\chi_{//}$ and $\chi_\perp$ are the magnetic susceptibilities of π spins in the antiferromagnetic state for the fields parallel and perpendicular to the easy axis, H_c is the spin-flop field of the π electrons, θ_D is the angle between the magnetic field and the direction of easy axis of molecule D, φ_D is the tilt of the torque vector of molecule D from the rotational axis. Similar expression can be defined for $\tau_C(H, \theta)$.

Figure 2 shows a simulation based on Eqs. (2) and (3). The consistency between the observation and calculation is satisfactory. The calculation demonstrates that the spin-flop field H_c is approximately given by the field where the torque at θ = 22.5° exhibits a minimum. Experimentally, this field is ~ 80 kOe at T = 9 K.

References
[1] N. Hanasaki *et al.*, Phys. Rev. B, **62**, 5839 (2000).
[2] N. Hanasaki *et al.*, J. Phys. Soc. Jpn. **72**, 3226 (2003).
[3] H. Tajima *et al.*, Phys. Rev. B, **78**, 064424 (2008).

Authors
H. Tajima, G. Yoshida, M. Matsuda, K. Nara[a], K. Kajita[a], Y. Nishio[a], N. Hanasaki[b], T. Naito[c], and T. Inabe[c]
[a]Toho University
[b]Okayama University
[c]Hokkaido University

Metallic Behavior Achieved by a Supramolecular Copper Complex with a Coordination of Oxidized Pyrazino-Fused Donors and Mixed Halide Anions as Ligands, $[Cu(I)Cl_{0.2}Br_{1.3}(pyra\text{-}TTF)^{0.5+}]$

Mori Group

The functional metal complexes to exhibit conductivity, magnetism, permittivity, optical response, and so on have attracted a great deal of interest. In particular, metal complexes with a coordination of functional molecular ligands have been intensively studied in view of multifunctionality for the magnetism of metal anions and the conductivity of redox ligands such as magnetic conductors. In order to explore more varieties beyond the limited acceptor ligands and broaden the range of d-π interactions, metal complexes with a coordination of "*donor*" ligands have been synthesized [1-4]. Herein, we report the successfully prepared supramolecular copper complex with a coordination of oxidized pyrazino-fused donors and mixed halide anions as ligands, $[Cu(I)Cl_{0.2}Br_{1.3}(pyra\text{-}TTF)^{0.5+}]$ (**1**) (pyra-TTF = pyrazino-tetrathiafulvalne) which reveals the metallic behavior down to 250 K.

Figure 1 shows the X-ray single crystal structure of **1**; Cu^{+} and $(Cl^{-}_{0.2}Br^{-}_{1.3})$ construct 1D supramolecular chains along the *c* axis, where a Cu(I) cation is directly coordinated by cationic pyra-$TTF^{0.5+}$. The mixed halides $(Cl^{-}_{0.2}Br^{-}_{1.3})$ are located at a normal position and an inversion center with positionally disorder in the complex. The compositions of the three samples investigated by crystal structure analyses are $Cu(I)Cl_xBr_y(pyra\text{-}TTF)$ [x = 0.160(6), y = 1.339(6); 0.207(8), 1.293(8); 0.21(1), 1.29(1)], namely $Cu(I)Cl_{0.2}Br_{1.3}(pyra\text{-}TTF)$. This framework of supramolecular mixed halide chains $[CuCl_{0.2}Br_{1.3}]_n$ constructs assembled donor ligand columns of **1**. The overlap integrals calculated by WinMOPAC (ver. 3.9.0, Fujitsu Limited) and band calculations suggest that this complex is a pseudo-one-dimensional conductor composed of dimerized donor ligands.

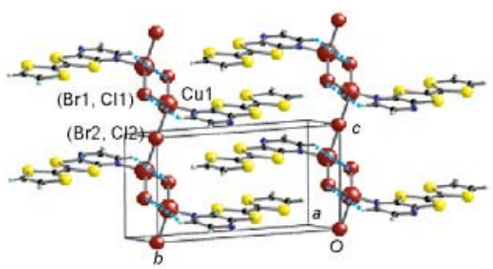

Fig. 1. Crystal structure of **1** (blue dotted line; (Br1,Cl1)…H1 contacts).

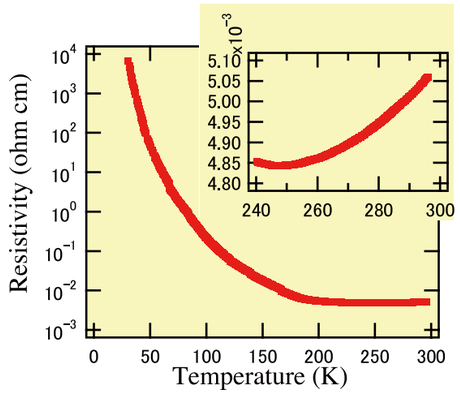

Fig. 2. Temperature dependence of resistivity for **1**.

The resistivity measurement was performed on single crystals with carbon paint as four-probe contacts. As shown in Fig. 2, **1** shows metallic behavior down to 250 K with σ_{rt} = 200 Scm^{-1}. The disorder of mixed halide anions might ease the dimerization of donor ligands and afford the metallic conduction paths; the average half-width of Bragg peak for the three metallic samples of **1**, $\Delta\omega$ = 0.49 °. The metallic behavior of **1** is first achieved among supramolecular metal complexes with a coordination of donor ligands. With lowering temperature, the resistivity gradually increases below 250 K (Ea = 6 meV), and drastically goes up at 190 K (Ea = 68 meV). The metal-insulator transition at 190 K is related to the low dimensionality of donor ligand columns.

ESR was measured with a Bruker EMS 9.3 GHz X-band ESR spectrometer at 300, 250 200, 150, 100, 50, and 4 K to investigate the oxidation state and the copper spin state of **1**. The g values are 2.013-2.014 from 300 K to 4 K; the complex has Cu(I) cations and the oxidized pyra-TTF. The decreases in the ESR line width ΔH and the intensity I ($\propto \Delta H^2 h$: h; height of estimated Lorentzian signals) were observed below 200 K.

To investigate the magnetic properties in detail, the temperature dependence of magnetic susceptibility for **1** was investigated by a Quantum Design MPMS-XL SQUID magnetometer under 10,000 Oe. The magnetic susceptibility χ after the subtraction of the Pascal diamagnetic contribution at 300 K is 1.26 × 10^{-4} emu mol^{-1}. From 300 K to 190 K, χ is constant, indicating the Pauli paramagnetism of the metallic characteristic, and below 190 K, χ decreases gradually to 0.63 x 10^{-4} emu mol^{-1} at 100 K, but remains half of

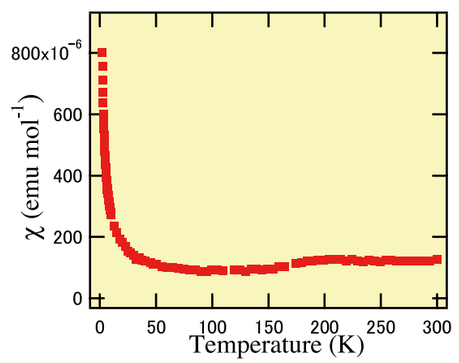

Fig. 3. Temperature dependence of magnetic susceptibility of **1**.

χ at room temperature (Fig. 3). This "imperfect" singlet state occurred because the instability of the low dimensionality is suppressed by the linked rigid supramolecular $(CuCl_{0.2}Br_{1.3})_n$ framework.

X-ray crystal structure analyses of **1** at low temperatures, 170 K and 120 K, were carried out to investigate the anomaly of the resistivity and magnetic susceptibility at 190 K. There were no drastic changes in either cell parameters and overlap integrals from 293 K, 170 K, to 120 K, or in superlattice below 190 K, indicating that the CDW (charge density wave) did not appear. The structures at every temperature are isostructural, where one donor and one unit of $(CuCl_{0.2}Br_{1.3})$ are crystallographically independent, suggesting no occurrence of a charge disproportion of donors. Moreover, the absence of a rapid increase in ΔH below 190 K, together with the constant g values of ESR signals at all temperatures, indicate no appearance of antiferromagnetic order. Therefore, the metal-insulator transition at 190 K might be caused by the incoherent tetramerization of donors to be partial singlet state. It is characteristic of supramolecular metal complexes that the coherent electronic and lattice instabilities to a complete singlet state are prohibited by the framework of $[CuCl_{0.2}Br_{1.3}]$ chains.

In conclusion, we succeeded in synthesizing a metallic supramolecular copper complex with a coordination to oxidized pyra-TTF and the mixed Cl^{-} and Br^{-} anions as ligands, $[Cu(I)Cl_{0.2}Br_{1.3}(pyra\text{-}TTF)^{0.5+}]$ (**1**). The assembled oxidized donor ligands create pseudo-1D conduction paths, since the dimerization of donor ligands is eased by the disorder of mixed halide anions. Then, **1** shows the metallic behavior down to 250 K and the increase in resistivity down to 190 K. Below 190 K, **1** is transformed into a semiconductor toward the partial singlet state, but the minimum susceptibility χ at 50 K remains half of χ at room temperature owing to the rigid framework of supramolecular copper halide chains $[CuCl_{0.2}Br_{1.3}]_n$. The introduction of a large variety of functionalities for coordinated ligands promises the development of new trends in functional metal complexes.

References
[1] S. Ichikawa, S. Kimura, H. Mori, G. Yoshida, and H. Tajima, Inorg. Chem. **45**, 7575 (2006).
[2] S. Ichikawa, S. Kimura, K. Takahashi, H. Mori, G. Yoshida, Y. Manabe, M. Matsuda, H. Tajima, and J. Yamaura, Inorg. Chem. **47**, 4140 (2008).
[3] S. Ichikawa, H. Mori, K. Takahashi, and J. Yamaura, Solid State Sci. **10**, 1724 (2008).
[4] S. Ichikawa and H. Mori, Inorg. Chem., to be publishedcv.

Authors
S. Ichikawa, K. Takahashi, and H. Mori

Quantum Criticality and Superconductivity in the New Heavy Fermion System β-$YbAlB_4$

Nakatsuji, Sakakibara, and Ishimoto Groups

A challenge for the standard model known as Fermi liquid theory is anomalous (non-Fermi-liquid) properties of metals and still rare but increasing number of unconventional superconductivity, both of which are often found in the vicinity of the quantum critical point, where a magnetic ordering temperature is driven to absolute zero by tuning a physical control parameter. These nontrivial collective phenomena are subtle and highly sensitive to sample purity and homogeneity of the environment, and thus the study of highly clean system under ambient conditions is ideal. For the study of such exotic phenomena, heavy-electron metals of 4*f* intermetallic compounds have provided prototype materials. An important issue concerning 4*f* intermetallics is the possibility of the parallelism between the physical properties of electron-like ($4f^1$ Ce) and hole-like ($4f^{13}$ Yb) compounds. The study of Ce and Yb materials indeed finds many similarities deriving from the antiferromagnetic coupling between the 4f magnetic moments and the conduction electrons (the Kondo screening) which leads to highly enhanced electronic effective masses at low temperatures. There has been however, a remarkable difference among their superconducting properties. While a number of Ce-based unconventional superconductors is found in the vicinity of a quantum critical point, in Yb-based heavy fermion compounds superconductivity has never been reported.

Recently, we have succeeded in synthesizing a new structural form of $YbAlB_4$, β-$YbAlB_4$ [1]. Our detailed work on the low temperature transport and thermodynamic properties of β-$YbAlB_4$ has revealed that this material is a rare example of a highly clean metal that displays quantum critical behavior at ambient pressure and under no applied magnetic fields [2]. Furthermore, we have discovered superconductivity in the quantum critical regime characterized by pronounced non-Fermi-liquid response [2,3].

The superconductivity is observed below T_c = 80 mK (Fig. 1). Interestingly, the system exhibits pronounced non-Fermi-liquid behavior above T_c, which is characterized by $T^{1.5}$ dependence of the resistivity (Fig. 1), $T^{-1/3}$ dependence of the susceptibility and logarithmic divergent electronic specific heat coefficient [2]. Furthermore, the magnetic field dependence of the non-Fermi-liquid behavior in Fig. 1 indicates that β-$YbAlB_4$ is a rare example of a pure metal that is quantum critical without tuning any physical parameter, *i.e.* without doping, applied pressure and magnetic field [2]. Our study using high-purity single

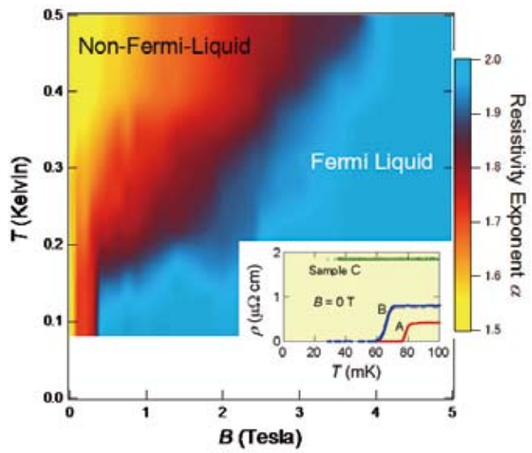

Fig. 1. Contour plot of the resistivity exponent α defined by $\Delta\rho = (\rho(T) - \rho(T)(0)) \sim T^{\alpha}$ in the temperature-field phase diagram [2]. Inset: Zero-field in-plane resistivity ρ_{ab} vs. T for various single crystals with different qualities, showing high sensitivity of T_c to sample purity. This indicates strong pair-breaking effects due to impurities, probably of nonmagnetic type, and suggests an unconventional character of the superconductivity [3].

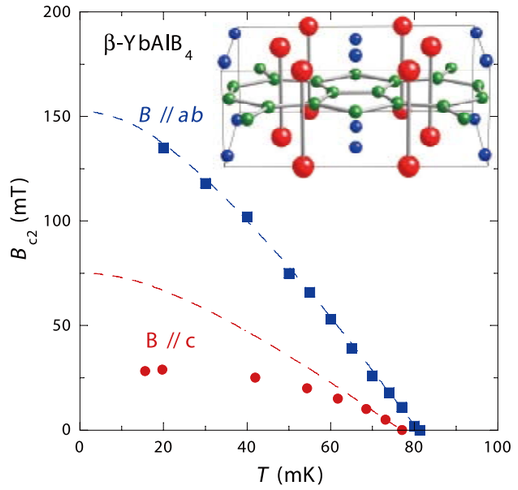

Fig. 2 Temperature dependence of the upper critical field B_{c2} along the *ab*-plane (square, blue) and the *c*-axis (circle, red)[3]. Different single crystals with similar T_c were used for each field direction measurement. Broken lines represent the curves obtained by fitting to the experimental results near T_c using the WHH model. Inset, the crystallographic unit cell of β-$YbAlB_4$ [1].

crystals indicates that the superconductivity is in the clean limit and most likely involves heavy quasi-particles [3]. Upper critical fields are anisotropic, and strongly suppressed for the field along the *c*-axis, possibly because of the paramagnetic effect due to the divergent *c*-axis susceptibility (Fig. 2). Strong sensitivity of T_c to sample purity suggests that the superconductivity is of an unconventional, non-*s*-wave type (Fig.1 inset).

References
[1] R. T. Macaluso, S. Nakatsuji, K. Kuga, E. L. Thomas, Y. Machida, Y. Maeno, Z. Fisk, and J. Y. Chan, Chem. Mater. **19**, 1918 (2007).
[2] S. Nakatsuji, K. Kuga, Y. Machida, T. Tayama, T. Sakakibara, Y. Karaki, H. Ishimoto, S. Yonezawa, Y. Maeno, E. Pearson, G. G. Lonzarich, L. Balicas, H. Lee, and Z. Fisk, Nature Phys. **4**, 603 (2008).
[3] K. Kuga, Y. Karaki, Y. Matsumoto, Y. Machida, and S. Nakatsuji, Phys. Rev. Lett. **101**, 137004 (2008).

Authors
S. Nakatsuji, K. Kuga, Y. Matsumoto, Y. Machida, T. Tayama, T. Sakakibara, Y. Karaki, and H. Ishimoto

Frequency Spectrum of an Anharmonic Ionic Vibration

K. Ueda Group

There is now growing interest in the anharmonic ionic vibrations in various materials which include the filled skutterudites, the intermetallic clathrates and the β-pyrochlore oxides. The anharmonic ionic vibrations are called rattling modes when the guest ions are oscillating in oversized cages. We are concerned with various unusual properties of the recently found superconductors in the β-pyrochlore compounds AOs_2O_6 (A = K, Rb, Cs).

As the size of the guest ions becomes smaller, the vibrational modes of alkaline ions show stronger anharmonicity which results in the lower frequency for KOs_2O_6 compared with $RbOs_2O_6$ and $CsOs_2O_6$. It is interesting to note that the transition temperature of the superconductivity is the highest for the K compound. The temperature dependence of the resistivity of the K compounds shows a strong concave-downward temperature dependence in contrast to the two other compounds where a usual T^2 dependence is observed.

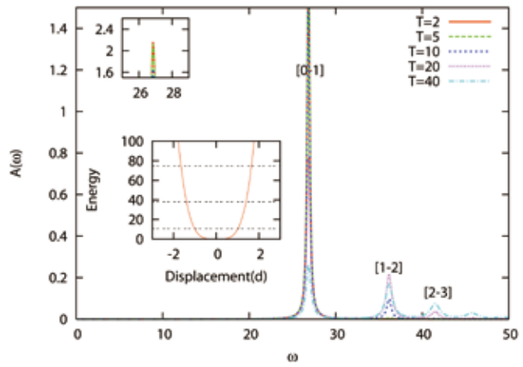

Fig. 1. Temperature dependence of the spectral weight of an oscillator in a quartic potential.

Recent experiments of NMR relaxation rates at the K site have been demonstrated to be entirely dominated by the vibrations of the K ion. Furthermore its temperature dependence has been found to be very anomalous, showing a peak at low temperatures and decreases towards high temperatures. To understand these unusual properties we studied the anharmonic lattice vibration coupled with conduction electrons by using the self-consistent harmonic approximation [1]. Subsequently, it was pointed out that the essence of the unusual behaviors lie in the fact that the spectral weight of vibrational modes shifts to higher energy side as the temperature is increased [2].

However the two treatments mentioned above assumed the phenomenological damping of the vibrational modes which may be justified only within the framework of the self-consistent harmonic approximation. In the present study we have investigated the phonon Green's function for any strength of anharmonicity within the second order perturbation theory with respect to the electron-phonon coupling. It is shown that for any type of anharmonicity the phonon Green's function is expressed by introducing a self-energy, a vertex correction and a renormalization constant for each transition between the two energy levels of the oscillator [3].

References
[1] T. Dahm and K. Ueda, Phys. Rev. Lett. **99** 187003 (2007).
[2] T. Dahm and K. Ueda, J. Phys. Chem. Solids **69** 3160 (2008).
[3] M. Takechi and K. Ueda, J. Phys. Soc. Jpn **78** 024604 (2009).

Authors
M. Takechi and K. Ueda

Effect of Coulomb Interaction for Shot Noise in a Quantum Dot

K. Ueda Group

Recent development of nanotechnology has enabled us to study the correlated transport in mesoscopic devices. Kondo effect in a quantum dot is a fascinating example. In this year, our group has investigated the shot noise for the Kondo effect in a quantum dot.

Recently shot noise in the Kondo regime has been studied. Especially in Refs.[1,2], the Fermi-liquid nature has been reexamined. They have considered the "backscattering current" I_b which expresses a reduction from the perfect transmission for the $\pi/2$ phase shift. It has been shown that the Fano factor $F_b = S/2eI$ results in a universal fractional value 5/3 up to V^3. This universal feature has stimulated further studies. A shot-noise measurement has been reported on 5/3 [3]. In the context of the full counting statistics[4] this result has been reproduced.

We have extended this result into any strength of Coulomb interaction by using the renormalization perturbation theory (RPT). Concerning shot noise, we have used the new formula of shot noise proposed in our recent study[5]. There, we have an expression of differential conductance: $G = \beta S/4 - \beta S_h/4$ where S is the current-current correlation function, and S_h is the non-trivial current-charge correlation function and $\beta = 1/k_BT$. We have called it the nonequilibrium Kubo formula. This is written into $S_h = S - 4k_BTG$. At zero temperature S_h equals the conventional shot noise S. In the linear response regime S_h is proven to vanish, and the Nyquist-Johnson relation is reproduced. Furthermore in noninteracting systems $S^0 - 4k_BTG^0$ expresses the known result of the shot noise. Therefore we have proposed that S_h gives a definition of shot noise at any temperature in correlated systems. Thus theoretically calculated S_h can be compared with $S - 4k_BTG$ using S and G measured in experiments. Therefore, the nonequilibrium Kubo formula enables us to address shot noise at any temperature in correlated systems [6]. We have applied this approach to the shot noise in a quantum dot. Then, the Fano factor has been estimated as

$F_b = 1+4(R-1)^2/[\,1+5(R-1)^2\,]$

where R is the Wilson ratio. Using limiting values of the Wilson ratio $R = 2$ in the Kondo limit, $F_b = 5/3$ is correctly derived. Therefore this expression gives the general expression in any Coulomb interaction strength [6].

References
[1] E. Sela, Y. Oreg, F von Oppen, and J. Koch, Phys. Rev. Lett. **97**, 086601 (2006).
[2] A. Golub, Phys. Rev. B **73**, 233310 (2006); ibid. **75**, 155313 (2007).
[3] O. Zarchin, M. Zaffalon, M. Heiblum, D. Mahalu, and V. Umansky, Phys. Rev. B **77**, 241303(R) (2008).
[4] A. O. Gogolin and A. Komnik, Phys. Rev. Lett. **97**, 016602 (2006).
[5] T. Fujii, J. Phys. Soc. Jpn. **76**, 044709 (2007).
[6] T. Fujii, submitted to J. Phys. Soc. Jpn. (2009).

Author
T. Fujii

Mechanism of Superconductivity in Graphite Intercalation Compounds (GICs)

Takada Group

In the study of the superconducting transition temperature T_c by *ab initio* calculations, the ultimate goal is to predict T_c by using only the information on elements composing superconductors. A less ambitious and yet very important goal is to make an accurate estimation of T_c directly from a microscopic Hamiltonian (in particular, without resort to the concept of the Coulomb pseudopotential μ^*), which helps us not only better understand the mechanism of superconductivity but also obtain valuable hints to synthesize a room-temperature superconductor.

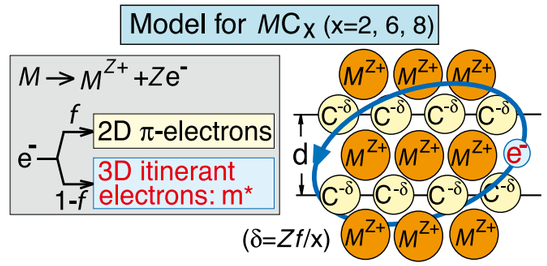

Fig. 1. In the GICs denoted by MC_x, the metal element M is ionized into M^{Z+} with Z the valence. The valence electrons released from M go into either the two-dimensional (2D) π-bands on the graphite layers or the three-dimensional (3D) interlayer band with the branching ratio of f : (1 - f). The 3D electrons with the effective mass m^* superconduct with the formation of the Cooper pairs mediated by the polarization waves of ions.

In pursuit of the latter goal, a proposal was made in 1978 for a scheme of calculating T_c directly from the dynamic electron-electron effective interaction $V(\boldsymbol{q}, \omega)$, including both the phonon-mediated attraction and the Coulomb repulsion on the same footing [1]. The scheme was successfully applied to the *n*-type semiconducting $SrTiO_3$ in which polar-coupled phonons leading to the stress-induced ferroelectrics were clarified to play a crucial role [2]. This success has assured us of both usefulness of this scheme and adequacy to employ the random-phase approximation in determining $V(\boldsymbol{q}, \omega)$ in the polar-phonon mechanism. In 1982 this scheme was also successfully applied to the alkali-doped GICs such as KC_8 and RbC_8 with T_c in the range 0.01-0.1 K by adopting such a model for the GICs as schematically shown in Fig. 1 [3].

In 2005, a breakthrough occurred in the field of the GIC superconductors. By changing alkali dopants into alkaline-earth ones in synthesizing the GICs, T_c was found to be very much enhanced. In CaC_6, for example, T_c = 11.5 K, which was increased further to 15.1K under pressures, and in YbC_6, T_c = 6.5 K. Note that T_c in CaC_6 is about a hundred times higher than that in KC_8, though the ion masses are about the same.

In order to check whether the same model in Fig. 1

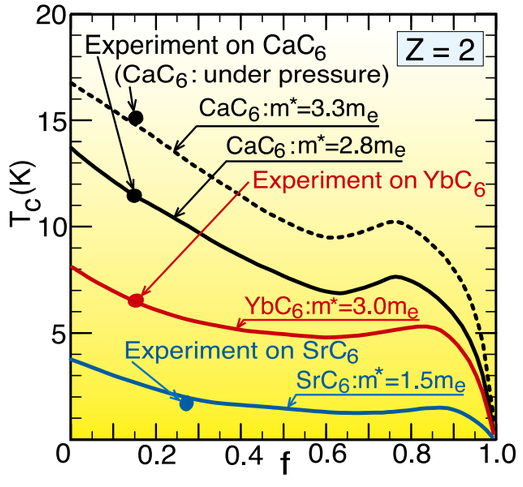

Fig. 2. Calculated T_c as a function of the branching ratio f. The calculation is done from first principles based on the model in Fig. 1 with using the band mass of the 3D electrons for m^*. The experimental result of T_c for each GIC is plotted at the value of f determined by the band-structure calculation.

applies to the newly-synthesized alkaline-earth-doped GIC superconductors or not, we have recently calculated T_c based on exactly the same scheme [4]. The parameters in the model have been changed appropriately for the new superconductors; for example, we have used Z = 2 instead of Z = 1, m^*~3m_e (due to the mixing of d electrons with the interlayer band) instead of $m^* = m_e$ (m_e: the mass of a free electron) and f = 0.16 (reflecting the stronger attractive potential of M^{2+} for the interlayer band) instead of f = 0.6. As shown in Fig. 2, we find that our calculations reproduce all the experimental results quite well, implying that our model must be a standard one representing all GIC superconductors with T_c ranging more than three orders of magnitude. Our calculations also reveal that the key parameters to control T_c are Z and m^*; the difference in T_c by two orders between KC_8 and CaC_6 can be accounted for by (1) doubling Z, which enhances T_c by one order, and (2) tripling m^*, which also enhances T_c by one order.

Encouraged by this success and with confidence in the predictive power of our standard model, we have estimated the optimum T_c in the GIC superconductors to find that T_c may become much higher than 10K, if M is chosen as Ti or V. A further enhancement of T_c, which might enter the range 50 - 100K, can be expected, if two or more kinds of Ms are suitably intercalated, so that both m^* and Z are made large enough and the polar-phonon energy is made as large as possible.

References
[1] Y. Takada, J. Phys. Soc. Jpn. **45**, 786 (1978).
[2] Y. Takada, J. Phys. Soc. Jpn. **49**, 1267 (1980).
[3] Y. Takada, J. Phys. Soc. Jpn. **51**, 63 (1982).
[4] Y. Takada, J. Phys. Soc. Jpn. **78**, 013703 (2009).

Author
Y. Takada

Pump Current Problem in Classical Stochastic Systems

Oshikawa Group

Fluctuations are abundant in our daily life. They are used efficiently in living matter in order to transmit information and substances. One of the famous examples of such phenomena is a Brownian motor or ratchet, in which the stochasticity plays an important role to obtain a unidirectional current of particles. In addition, understanding of the

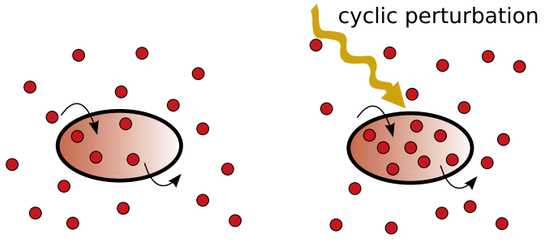

Fig. 1. An illustrative example of pump current problem induced by cyclic perturbations. Many ions are absorbed into or emitted from a red blood cell through ion pumps, and the ion concentrations in the cell are maintained constant. When a cyclic perturbation (electric field) is applied, the pumping mode is activated, and the ion concentrations in the cell are changed.

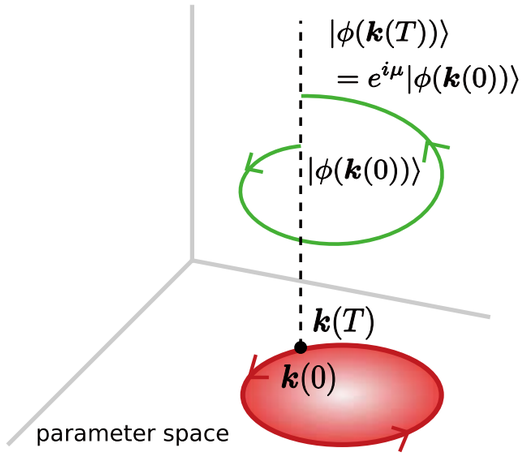

Fig. 2. Phase shift due to the cyclic motion in the parameter space. Cyclic perturbations make a closed loop in the parameter space. In contrast, the state vector obtains an additional phase μ after one cycle of the perturbations. This phase gives a net current of the system. In addition, the area of the red circle in the parameter space is related to the magnitude of the pump current.

stochasticity in microscopic or mesoscopic systems would greatly benefit future developments of nanotechnology.

A net current induced by periodic perturbations is known as a pump current, which is a typical problem of nonequilibrium physics. There are several experiments for the pump current problem. In one of the experiments, red blood cells are exposed to an oscillating electric field. Figure 1 shows an illustrative explanation for the experiments. The red blood cell maintains its intracellular sodium and potassium ion composition relatively constant because of the ion transfer activity of an enzyme called (Na, K)-ATPase in the cell membrane. It has been shown that the pumping function of the enzyme is activated due to the oscillating electric field. The ion transfer is in fact a stochastic phenomenon, and the experiments imply that cyclic perturbations can control particle currents using the stochasticity of the system.

A simple stochastic model with particle hopping has already been proposed, which shows a pump current due to periodic perturbations to transition rates. A pump current and its fluctuations have been calculated in an adiabatic regime, where the periodic perturbations change slowly. However, the experiments are actually carried out also in the non-adiabatic regime, where the time scales of particle movements and external perturbations are comparable. This calls for theoretical advancements on the non-adiabatic regime.

We developed a new theoretical approach based on a mathematical analogy to quantum mechanics, although we study a classical stochastic model. By using a generalization of the non-adiabatic geometrical phase in quantum mechanics called as Aharonov-Anandan phase, we succeeded in calculation of all the current statistics even in the non-adiabatic regime [1, 2]. It was shown that the qualitative behavior of the average current is consistent with the experimental one; the current shows stochastic resonance behavior and power-law decay with respect to the frequency of the external perturbations. The geometrical phase interpretation also leads to an intuitive understanding of the condition to observe a non-vanishing pump current. A periodic change in time of the model parameters, such as hopping rates, can be represented by a closed loop in the parameter space, as shown in Fig. 2. While the model parameters come back to the initial value after one cycle, the final state vector after the cycle is in general different from the initial one; the state vector obtains an additional phase after the cycle, as in the case of quantum mechanics. The additional phase gives all the statistics of the pump current. In addition, the area in the parameter space enclosed by the loop is related to the magnitude of the pump current. This implies that there is no pump current when there is only one parameter change; in this case, a line is depicted in the parameter space, and the area of the line is zero.

The key point of this work is the analogy to the geometrical phase in quantum mechanics. Precisely speaking, our model does not map to a standard quantum mechanical problem, since the 'Hamiltonian' is non-Hermitian. Nevertheless, many techniques and concepts developed in quantum mechanics and condensed matter physics can be applied. The present approach opens a path to deeper understanding of classical stochastic systems in the future.

References
[1] J. Ohkubo, J. Stat. Mech., P02011 (2008).
[2] J. Ohkubo, J. Chem. Phys. **129**, 205102 (2008).

Author
J. Ohkubo

Nonadiabatic Electron-Nucleus Dynamics from Time Dependent Density Functional Theory

Sugino Group

Modern electronic structure theories are mostly based on the Born-Oppenheimer (BO) approximation to decouple the electrons and nuclei, but even with their large mass asymmetry this approximation breaks down when nearly degenerate adiabatic states strongly couple with each other. The coupled electrons and nuclei exhibit nonadiabatic dynamics, which is a hot topic of ultrafast laser science. The dynamics is described by the BO surfaces and their nonadiabatic couplings (NACs), and thus their accurate evaluation is a starting point of theoretical study. Here we have developed a feasible scheme to compute the first order NAC, or the NAC vector, which had been available only through a time-consuming quantum chemical method. Using the NAC vectors calculated for the formaldimine molecule (CH_2=NH) we have simulated the photo-isomerization process and obtained the quantum yield.

Our method is formulated within the time-dependent density functional theory (TD-DFT) and is based on the adiabatic local density approximation (ALDA) for the exchange and correlation of the electrons, but no further approximations are used for the electrons contrary to similar existing methods. TD-DFT is a scheme to compute the response of the electrons to an external perturbation, and when the electrons are perturbed by displacing a nuclear position, the response contains information on the NAC; this provides a means to compute NAC from TD-DFT. When an algebraic equation is derived to obtain NAC, the calculation has made extremely simple and robust [1]. Indeed, NAC of the formaldimine molecule could be computed on mesh points of nuclear coordinate (Fig. 1) and along the nuclear

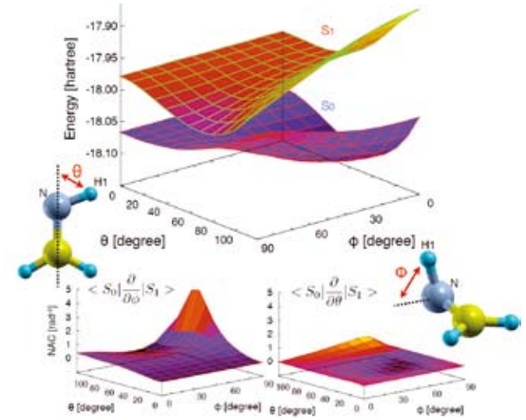

Fig. 1. Born-Oppenheimer surfaces of formaldimine (CH_2=NH) in the coordinate space (φ, θ) , for the ground state (S0) and the first excited state (S1). The First order nonadiabatic couplings (NACs) are also shown at the bottom.

trajectory allowing, respectively, full quantum wavepacket simulations and semiclassical surface hopping simulation.

Figure 1 shows the potential energy surface of the ground state (S_0) and the first excited state (S_1) of the formaldimine. Other excited states are separated in energy and thus low energy dynamics concerns these surfaces only. Because of this property, the second order NAC can be obtained from the first order NAC [1], which enables to conduct a legitimate full quantum wavepacket simulation. As seen in the figure, value of the first-order NAC is much larger for the twisting direction (φ) than for the inversion direction (θ). With this asymmetry in mind the wavepacket simulation was conducted along φ. As φ increases from 0°, which corresponds to the Frank-Condon excited geometry, to 90°, which corresponds the pseudocrossing point which is located at a midway between the initial and isomerized geometries, a nonadiabatic transition occurs. The branching ratio, or the probability of being on the ground state versus that remaining on the exited state after the transition, is 0.53. The component of the wavepacket remained on the excited state proceeds further in the φ direction but the group velocity is reversed at the classical turning point and the second transition occurs at 90°. After these transitions, 70% of the state is found isomerized. When the simulation is done using full degrees of freedom semiclassically, the dynamics is characterized by two dimensional motion in (φ, θ), and the quantum yield becomes finally 0.47

The application is presently limited to the transition between the ground state and an excited state (DFT-restriction) and the excitation should be of one-electron character (ALDA-restriction). The quantum dissipation effect needs to be accurately described as well. In spite of them, our simulation has advance a step towards a realistic excited state dynamics which has been very rarely studied from first-principles.

References
[1] C. P. Hu, H. Hirai, and O. Sugino, J. Chem. Phys. **127**, 064103 (2007).
[2] H. Hirai and O. Sugino, Phys. Chem. Chem. Phys. **11**, 4570 (2009).

Authors
H. Hirai, CP. Hu[a], and O. Sugino
[a]National Institute for Materials Science

Enhanced Spin Susceptibility toward the Charge-Ordering Transition

Kato Group

Charge-ordering (CO) transition in organic conductors has attracted much interest as emergence of strong correlation effect induced by long-range Coulomb interaction. Many CO materials show a sharp metal-insulator transition characterized by a rapid exponential increase of resistivity below the metal-insulator transition temperature T_{MI}. In contrast to remarkable change in the charge degree of freedom, the spin susceptibility is frequently less sensitive to the CO transition, but exhibits non-trivial dependence on temperature. For example, the spin susceptibility of θ-(BEDT-TTF)$_2$RbZn(SCN)$_4$, which is a typical CO material, has a broad peak around T_{MI} without any sign of singularity. In the weak-coupling theory like random phase approximation (RPA), the CO transition is described from the metallic side by divergent development of charge fluctuation at a finite wave number corresponding to charge pattern in the CO phase. Is it possible to understand gradual increase of the spin susceptibility toward the CO transition by development of charge fluctuation? In order to answer this question, RPA is unsuitable because the spin susceptibility in RPA is not affected at all by charge fluctuation. Therefore, we have to go beyond RPA by considering the vertex corrections for describing coupling between charge and spin fluctuations.

We have studied response functions up to leading contribution of vertex corrections in a two-dimensional extended Hubbard model [1, 2]. We have formulated an iterative method for producing a series of the non-skeleton diagrammatic expansions within the framework of Baym-Kadanoff conserving approximation, and have used the first step of this non-skeleton conserving approximation (1NSCA). In Fig. 1, we show the spin susceptibility as a function of the nearest-neighbor Coulomb interaction V. The temperature and the on-site Coulomb interaction are taken as $T = 0.1$ and $U = 3$, respectively. The spin susceptibility is gradually enhanced toward the CO transition point at $V = V_{CO}$. 1NSCA consists of a sum of three diagrams for the irreducible response function as shown in the figure: The self-energy correction (SC), the Maki-Thompson vertex correction (MT), and the Asmalazov-Larkin (AL) vertex correction. In our calculation, the AL vertex correction is responsible for enhancement of the spin susceptibility.

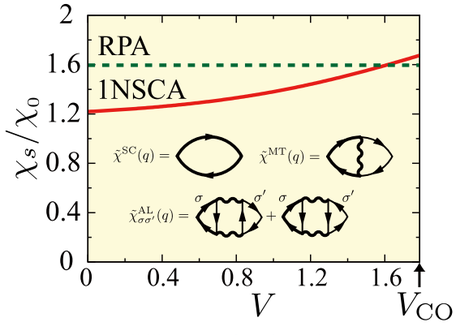

Fig. 1. Spin susceptibility as a function of the nearest-neighbor Coulomb interaction V for $T = 0.1$ and $U = 3$. Susceptibility is normalized by the Pauli susceptibility of noninteracting electron systems. Three types of diagrams treated in the present calculation are also shown.

Our result is consistent with experimental measurement of the spin susceptibility for the organic CO materials, θ-(BEDT-TTF)$_2$RbZn(SCN)$_4$ and β-(*meso*-DMBEDT-TTF)$_2$PF$_6$. We also speculate that the spin susceptibility of inorganic CO materials such as β-$Na_{0.33}V_2O_5$ may be explained by our theory. Detailed comparison between theory and experiment is a future problem. We note that the spin susceptibility is *suppressed* by antiferromagnetic spin fluctuation [3]. Our study of the spin susceptibility in the CO materials will give a fundamental insight to the interplay of the spin and charge degree of freedom in strongly interacting electron systems.

References

[1] K. Yoshimi, Ph. D Thesis, University of Tokyo (2009).
[2] K. Yoshimi, T. Kato, and H. Maebashi, submitted to J. Phys. Soc. Jpn.
[3] Y. Fuseya, H. Maebashi, S. Yotsuhashi, and K. Miyake, J. Phys. Soc. Jpn. **69**, 2158 (2000).

Authors

K. Yoshimi[a], T. Kato, H. Maebashi

[a]College of Liberal Arts and Sciences, Tokyo Medical and Dental University

Micro-Hall Magnetometry for the Study of Vortex State in Mesoscopic Superconductor

Iye Group

When a magnetic field is applied to a clean bulk type-II superconductor, quantized vortices form the so-called Abrikosov lattice. In a mesoscopic superconductor with dimensions comparable to the characteristic length scales of the superconductor, the vortex state is determined by the subtle interplay among the vortex interactions with other vortices, with the system boundaries and possibly with defects. Theoretically, this constitutes an interesting and well-defined oligo-body problem.

We have developed a multi-probe micro-Hall device fabricated from a GaAs/AlGaAs two-dimensional electron gas (shown in Fig. 1) that can be used for non-invasive local magnetometry. The Hall cross consisted of channels in a 3 × 3 matrix form. The superconducting sample to be investigated is placed at an appropriate position near the Hall cross.

Measurement of the Hall resistances R_{xy} for different combinations of the current- and voltage-leads provides information on the local magnetic field distribution.

A mesoscopic superconductor (a square sheet of Al with 4 holes at the corners) was placed on top of the Hall cross. The purpose of 4 holes was to stabilize the configuration of 4 vortices and to explore the possible occurrence of an antivortex. Traces in Fig. 2 show the changes in the local magnetic induction averaged over each of the 3 × 3 sub-areas of the Hall cross as the external field is swept up from a negative value. Steps in these traces signal the change in the vortex state. Starting from the Meissner state near $H = 0$, vortices enter one by one.

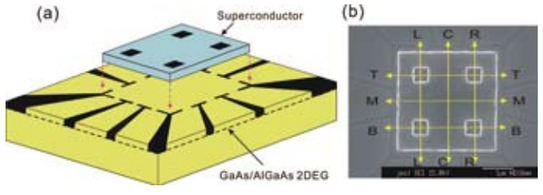

Fig. 1. (a) Schematic drawing of the multi-probe micro-Hall device. The superconducting sample to be studied is placed on top. (b) SEM image of the sample.

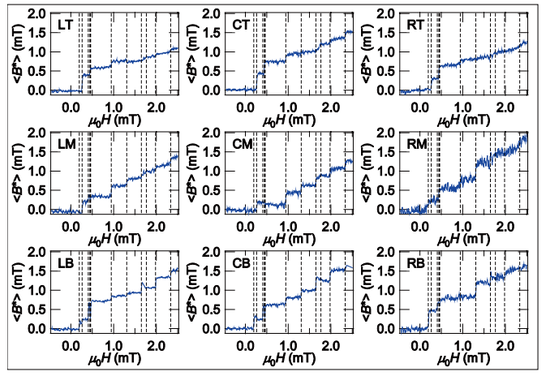

Fig. 2. Change of the average local magnetic induction in each of the 3 × 3 sub-areas of the Hall cross. The steps in the traces signal changes of the vortex configuration in the mesoscopic superconductor.

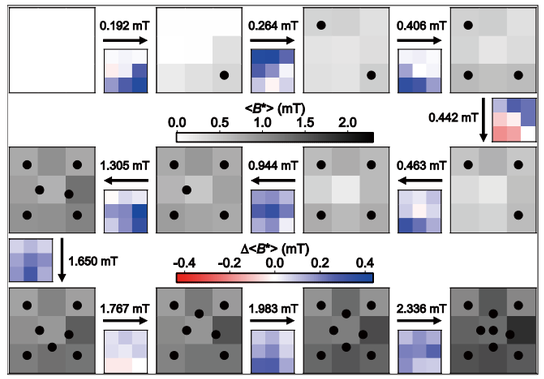

Fig.3 Sequencial changes of the magnetic field distribution. The smaller figures represent the difference between two successive states. The vortex configurations shown with the solid dots are reconstructed from the data.

Figure 3 shows the evolution of the vortex configuration reconstructed from the data in Fig. 2. The first four vortices are trapped at the holes near the corners. The stability of the 4- vortex state is reflected in the width of the corresponding plateaus in Fig. 2. It is interesting that there occurs reconfiguration of the 3-vortex state at $H = 0.442$mT . Similar reconfiguration is also seen for the 7-vortex state at $H = 1.767$mT.

To summarize, we have developed a multi-probe micro-Hall device with decent spatial resolution that enables us to trace the evolution of the vortex state. With the sufficient detection sensitivity, the occurrence of an antivortex in the present sample was ruled out.

Reference

[1] H. Sano, A. Endo, S. Katsumoto, and Y. Iye, submitted to Appl. Phys. Lett.

Authors

H. Sano, A. Endo, S. Katsumoto, and Y. Iye

Quantum Dot Spin Detector

Katsumoto Group

Electron spin is a promised candidate of a freedom to be used in next-generation devices such as quantum-bits or “spintronics” devices. A key technique to realize such devices is highly sensitive detection of electron spin polarization. However compared with charge (monopole) imbalance, which can be easily detected through the flinging electric field, detection of spin polarization through the flinging magnetic field is very difficult due to the dipole nature of spin. Hence, usually spin-polarization in solids is detected through electric transport entangled with spin polarization, which inevitably affects the spin sources. Such strong disturbance is usually fatal for fragile spin sources such as spin-orbit polarization creators in non-magnetic semiconductors. We have developed a highly sensitive method of spin-polarization detection through excited state spectroscopy with least disturbance to target devices.

Figure 1 is displaying the device setup on a scanning electron micrograph. A quantum dot (QD) with a plunger gate is coupled to a side of a quantum wire and the flinging electric field from this set is detected by a quantum point contact (QPC) put just aside of the dot. In measurements, the electro-chemical potential of the dot is periodically swung up and down by the plunger gate voltage (V_p). This oscillation of the gate causes that of electric field which is synchronously detected by the QPC. When the base level of V_p is shifted and a discrete energy level comes into the oscillation window, single electrons begin shuttling between the wire and the dot through quantum tunneling. The shuttle motion screens the oscillation of the fringe field resulting in the diminishment of the signal, through which the tunneling probability as well as the level position can be detected.

Now we prepare an electronic state which can accommodate only an electron with a spin of certain direction, then the tunneling probability is determined by the product of orbital wavefunction overlapping and spin-direction projection due to the Pauli principle. Such preparation can be performed by various methods, *e.g.*, by using two sequential pulses on V_p with different depths yields signal, which has monotonic correspondence with spin polarization.

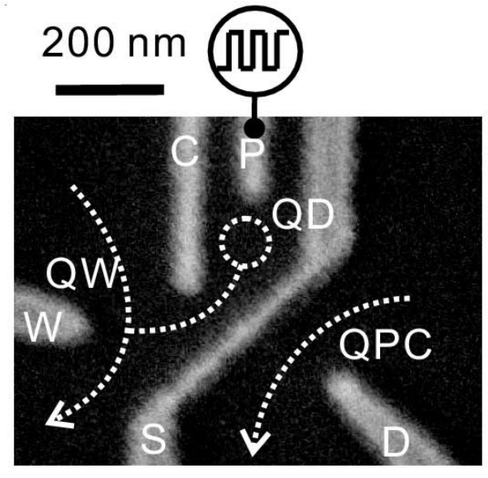

Fig. 1. Scanning electron micrograph of the device setup showing QD (quantum dot), QW (quantum wire), QPC (quantum point contact). P is the plunger gate, to which rectangular wave voltage is applied.

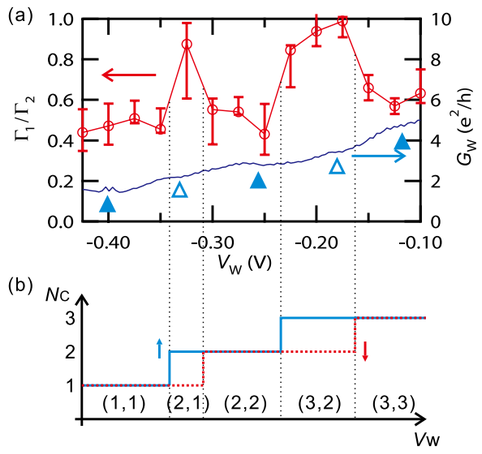

Fig. 2. (a) Measured spin polarization Γ_1/Γ_2 (red line) and the wire conductance (blue curve) as a function of wire gate voltage. Filled triangles indicate conductance plateau with even conductance quanta (n: even) while open ones those with odd. (b) Number of conductance channels for up (cyan) and down (red) spins.

We have applied the above method to detect spin polarization in quantum wire placed in strong magnetic field parallel to the two-dimensional electron gas, which forms the wire. The parallel field causes the Zeeman splitting both inside the wire and the dot. Combination of the former split and the control of the wire gate voltage can switch on and off the spin polarization in the wire. On the other hand, the latter split automatically fixes the spin state in QD, hence simple rectangular wave oscillation of V_p can produce the spin-polarization signal. Figure 2 shows the wire conductance and thus measured spin polarization as a function of the wire gate voltage. As a consequence of transverse mode formation, the wire conductance is quantized to $n(e^2/h)$, where n is an integer, e the electron charge, h the Planck constant. The spin polarization should appear when n is an odd integer and disappear for evens. Such behavior indeed appears in Fig.2 confirming that the proposed detection is really working.

Authors
S. Katsumoto, T. Otsuka, and E. Abe

Atomic Switch for Scattering Phase of Electrons at Ge (001) Surface

Komori Group

An electron changes its phase when it is scattered by an atomic potential. The scattering phase shift can be detected on the metal and semiconductor surfaces by observing the electron standing wave in the differential conductance (dI/dV) image using scanning tunneling microscopy (STM). We have studied the reflection phase of one-dimensional (1D) electrons at four kinds of atomic potentials on the clean Ge(001) surface. The clean Ge surface consists of buckled dimers, which align in the [110] direction and form dimer rows. The empty π*-band electrons of the surface Ge dimers behave like 1D free electrons along the dimer row. We measured the π*-band standing waves around the buckled dimer with one Si or Sn atoms in the differential conductance images at various sample-bias voltages.

Figure 1 shows the topographic STM images of the Si-Ge dimers on the surface at 80 K. Two kinds of buckled dimers with a Si atom at either the upper or lower position (Si U- and L-dimers) are made by deposition of Si atoms on the clean surface at room temperature as in the models. These dimers can be distinguished by observing their sample-bias dependence. Standing waves appear and decay from the both kinds of the impurity dimer. The cross sections of the dI/dV images from the Si-Ge dimers are shown in Figs. 2(a). The standing waves due to a Sn-Ge L-dimer with a Sn atom at the lower position (Sn L-dimer) [1] are shown in Fig. 2(b) for comparison. The scattering phase of Si L-dimer has the sign opposite to those of Sn L-dimer and Si U-dimer. The results indicate the scattering potential by Si L-dimer is attractive while the potentials due to other two impurity dimers are repulsive. The signs of the scattering potential are reproduced by first-principles calculations. The

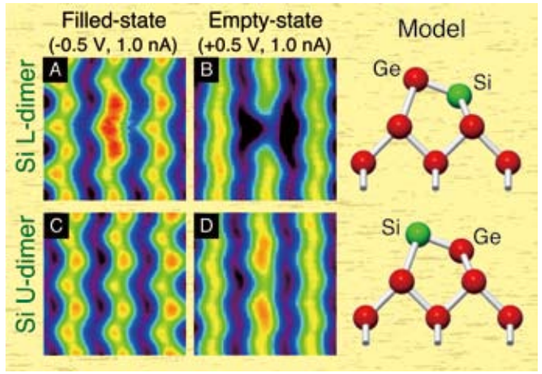

Fig. 1. Topographic (A-D) STM images of Si U- and L-dimers on the Ge(001) surface at 80 K for two sample-bias voltages ± 0.5 V. At + 0.5 V, the both dimers are lower than the pure Ge dimer while at - 0.5 V, Si L(U)-dimer is higher than (has the same apparent height as) the pure Ge dimer. We identified the both dimers by comparing these STM images with the local electronic states obtained by DFT calculations for their optimized atomic structures. The corresponding schematic models for the dimers are given in the left column.

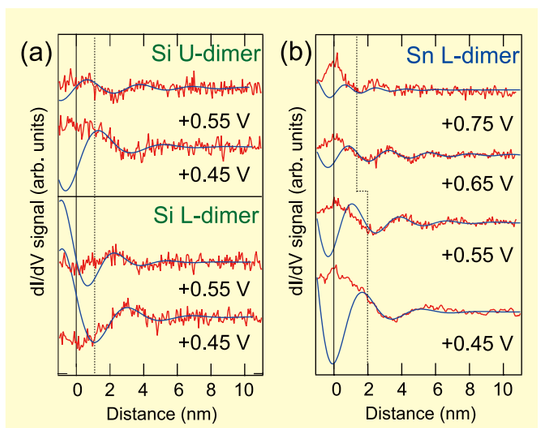

Fig. 2. Red curves are cross sections of the standing waves of the 1D π* electrons in the dI/dV images for Si L- and U-dimers (a) and Sn L-dimer (b) at several sample bias voltages. The data were obtained at 80 K. The dimer is at the origin of the abscissa in each figure. Each blue curve is the damping oscillation fitted to each red curve. For the fitting, we used the dispersion relation of the π*-band obtained on the clean surface.

difference between Si and Sn L-dimers is attributed simply to energy difference of the valence p_z states among Si, Ge and Sn atoms. [2] We are able to transform one kind of the Si-Ge dimer to the other kind reversibly by changing the bias polarity together with the buckling orientation of all the Ge dimers in the dimer row including the impurity dimer. Thus, using the Si-Ge dimer, we have realized a scattering phase switch in an atomic scale.

References
[1] K. Tomatsu, K. Nakatsuji, T. Iimori, Y. Takagi, H. Kusuhara, A. Ishii, and F. Komori, Science **315**, 1696 (2007).
[2] K. Tomatsu, B. Yan, C. Wang, M.Yamada, K. Nakatsuji, G. Zhou, W. Duan, and F. Komori, Phys. Rev. B **78**, 081401(R) (2008).

Authors
K. Tomatsu, B. Yan[a], M. Yamada, K. Nakatsuji, W. Duan[a], and F. Komori
[a]Tsinghua University

Vortices in Nano-sized Superconductors and their Size Effect

Hasegawa Group

When type-II superconductors are subjected to an external magnetic field, quantized magnetic fluxes or vortices each with a radius of the coherence length ξ are formed. Using a ^{3}He-cooled low-temperature scanning tunneling microscopy (STM), we studied the vortex formation in nano-sized superconductors whose sizes are in an order of ξ to investigate the size dependence of the vortex formation [1].

Lead is one of the elemental superconductors, whose critical temperature is rather high (7.2K). We deposited Pb on a Si(111) substrate and formed island structures whose typical sizes are 25-75 nm in radius and 3 nm (9 monolayers) in thickness with an atomically flat surface. The coherence length of the Pb thin film is ~ 31 nm at 2.0 K. Because of a short mean free pass limited by the thickness, the Pb thin

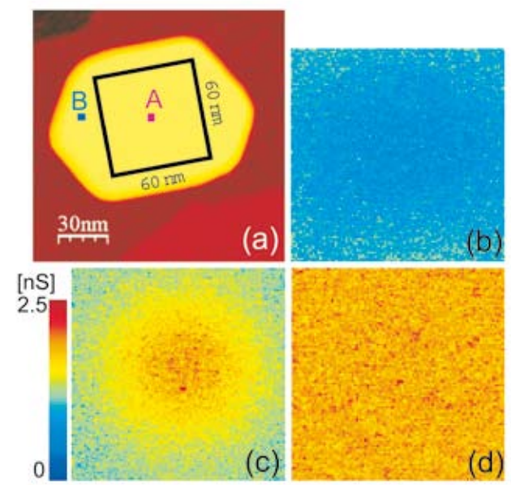

Fig. 1. (a) STM image of a Pb island whose thickness is 3 nm. (b-d) ZBC images taken in the black square area of (a) at 2.0K under magnetic fields below the vortex formation (b, 0.5T), just above the vortex formation (c, 0.6 T), and above the super-normal transition (d, 0.9 T). A vortex is clearly visible around the center in (c).

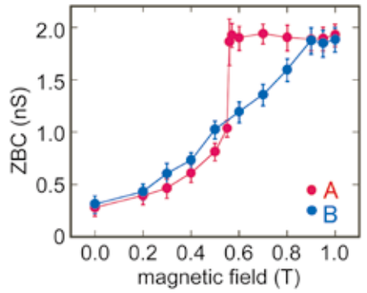

Fig. 2. ZBC measured at two sites A and B marked in Fig. 1(a) under various magnetic fields. The jump observed at A corresponds to the vortex formation.

films are type-II superconductors whereas bulk Pb is type-I.

Figure 1 shows an STM image (a) taken on a Pb island whose radius is ~ 55 nm and tunneling conductance images (b-d) taken at the zero bias voltage under various magnetic fields perpendicular to the island's surface. Since the zero-bias conductance (ZBC) is correlated with the density of states (DOS) at the Fermi level induced by the Cooper-pair breaking, higher ZBC indicates lower pair potential (order parameter). Slightly large ZBC area in the peripheral of the Fig. 1(b) image, which was taken at 0.5T, is explained with supercurrent circulating there. The ZBC image taken at 0.6 T (c) shows high ZBC area around the center. It is indeed confirmed as a vortex since its cross-sectional profile was well fitted with the calculated DOS around a vortex using the Eilenberger equation. At 1.0 T (d), the ZBC values are quite high in the whole area implying complete breakdown of the superconductivity in the island.

We also measured ZBC as a function of the magnetic field at the center of the island (A) and a peripheral site (B) 40 nm away from the center. In the profile shown in Fig. 2, a jump corresponding to the vortex formation is observed at site A around 0.6 T whereas at site B ZBC increases monotonically with the field until saturated at 0.9 T. Around the vortex penetration field we also observed a hysteresis of ZBC and it is explained with an energy barrier, called the Bean-Livingston barrier, existing in the peripheral of the islands, which the vortex needs to overcome for the penetration (expulsion) into (from) the island.

Since the magnetic fields for the vortex penetration / expulsion can directly be measured for each island from a ZBC vs. magnetic field curve like the one shown in Fig. 2, we examined their lateral size dependence. It is found that larger islands have lower critical fields and that there is a minimum lateral island size for the vortex penetration. These findings were explained with the theoretical calculations based on the Ginzburg-Landau equations, and the experimentally obtained minimum size was consistent with the estimated one by the theory [2].

References
[1] T. Nishio *et al*., Phys. Rev. Lett. **101**, 167001 (2008).
[2] V. A. Schweigert *et al*., Phys. Rev. B **57**, 13817 (1998).

Authors
T. Nishio, T. An, T. Eguchi, H. Sakata[a], S. Lin[b], N. Hayashi[c], N. Nakai[c], M. Machida[c], and Y. Hasegawa
[a]Tokyo University of Science
[b]National Institute for Materials Science
[c]Japan Atomic Energy Agency

Ruddlesden-Popper Quantum Wells

Lippmaa Group

Several different approaches have been proposed for fabricating two-dimensional oxide quantum wells. In most cases, the techniques known from traditional semiconductors have been applied to oxides. However, epitaxial oxide heterojunctions or superlattices do not generally show good carrier confinement. One of the main reasons for this is the complicated structural and electronic distortions that occur at oxide heterointerfaces. Charge transfer across an interface and the formation of very thick depletion layers mean that quantum well structures that offer excellent structural confinement do not generally provide good electronic confinement.

We are attempting to solve this problem by fabricating a quantum well that combines a cubic perovskite lattice with a Ruddlesden-Popper (RP) phase. This combination is similar to a bulk RP material with the exception that we embed only a single RP formula unit in a perovskite matrix, as illustrated in Fig. 1.

This structure has several advantages over a simple perovskite heterojunction. The center part of the well structure has the same cation coordination and lattice parameter as the matrix material, but it is isolated from the matrix by rocksalt layers on both sides. The rocksalt layers provide both electronic confinement and ionic confinement, i.e. the structure can be thermodynamically stable and thus resistant to cation interdiffusion.

An essential part of growing such structures is the ability to monitor the growth of each atomic layer. We do this by measuring the intensity of the specular reflection in a reflection high-energy electron diffraction pattern. The intensity variation with time (Fig. 2) shows that we can indeed observe the formation of each perovskite and rocksalt block.

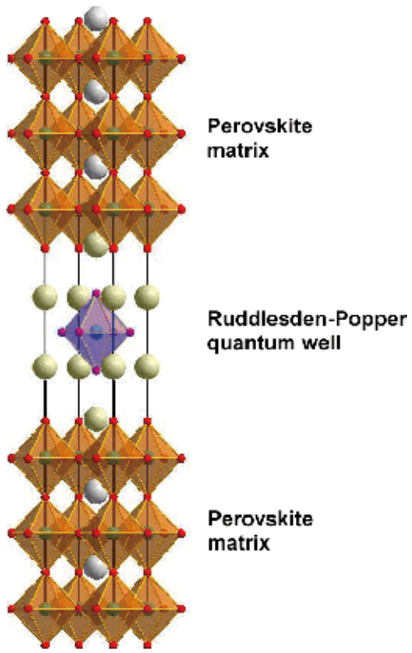

Fig. 1. Structure of a quantum well formed by embedding a single Ruddlesden-Popper formula unit layer in a perovskite matrix.

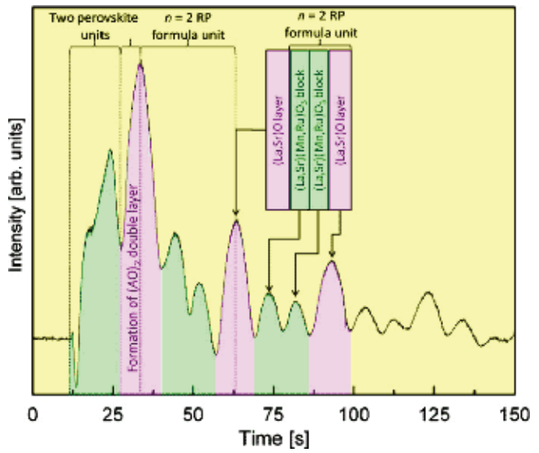

Fig. 2. Specular RHEED intensity during the growth of a $La_{1.2}Sr_{1.8}Mn_{1.7}Ru_{0.3}O_7$ film. The alternating sequence of rocksalt (La,Sr)O and perovskite (La,Sr)(Ru,Mn)O_7 blocks can be seen. In this case, the growth started with the formation of a double perovskite block at the interface.

In this example, a $La_{1.2}Sr_{1.8}Mn_{1.7}Ru_{0.3}O_7$ film was grown on a $SrTiO_3$ surface. By suitable buffering of $SrTiO_3$ substrate surface with a fractional layer of (La,Sr)O, it is possible to choose which block forms at the initial interface, either a perovskite unit or a rocksalt unit.

Reference
[1] M. Matvejeff, T. Chikyow, and M. Lippmaa, Journal of Crystal Growth **311**, 1201 (2009).

Authors
M. Matvejeff, M. Lippmaa, and T. Chikyow[a]
[a]National Institute for Materials Science

Vortex Physics in hcp solid ^{4}He and a new development of Superfluidity Study

Kubota Group

The report of the Kubota group on the evidence for quantized vortices and the vortex fluid (VF) state [1] has been stirring the low temperature community. Additional reports on the possible transition from VF state into a 3D supersolid(SS) state [2] are further exciting the community, although there is neither a microscopic theory nor common understanding of the description of all the experimental observations reported so far for the solid ^{4}He.

Proposals for the existence of supersolid state in a quantum solid, solid ^{4}He go back to the 1960's. The reason for expecting such a peculiar state of coexistence of order in real space, the lattice structure of the solid, combined with simultaneous order in momentum space, as required for the superfluidity, is based on the fact that disorder, actually, vacancies and interstitials should exist to some extent even at absolute zero temperature in some quantum solids on account of the large zero point motions. Since the time when the "classical proposals" were made around 1970 [3], there have been substantial experimental efforts exerted to discover such a state over more than 35 years, before Kim and Chan announced their first "possible non-classical rotational inertia"(NCRI) observation in solid ^{4}He samples formed in Vycor porous glass in January 2004 [4] by torsional oscillator(TO) technique. They reported also results with bulk torous samples [5] with and without a blockage to test the macroscopic features of the observation. Confirmation of Kim and Chan's experimental observations by other groups took quite some time and it was around the beginning of 2006, when other groups including the Kubota group started reporting similar results. This was because the features of the phenomena are quite sensitive to very small ac excitation velocities in the TO experiments. As little as 10μm/s linear speed seemed to cause decrease of the TO signals substantially. It was, however, also becoming problematic to expect BEC of any quasi particles(vacancies or interstitials) or other excitations at 200 mK or so as reported by Kim and Chan [4,5] considering the known densities of these excitations.

It was P. W. Anderson, who proposed the vortex fluid scenario [6] for the experimental observations reported till 2007. His point is as follows; the reported "onset temperature" of 200mK [4] to 500 mK [1] is too high to expect BEC to occur from the knowledge of number density of vacancies or interstitials and reported logV_{ac} linear dependence [4,5], where V_{ac} is the linear velocity at the torsion pendulum edge. This indicates involvement of vortex lines in the observation. He also pointed out that the reported TO results would represent non-linear rotational susceptibility(NLRS) of the VF state [6].

Penzev, *et al.*, [1] reported a clear finding of the onset temperature T_o at 500 mK for samples at 32 and 49 bar pressure, the highest T_o ever reported for solid ^{4}He, where significant V_{ac} dependence starts to appear. The TO response of solid ^{4}He has a unique feature, which is opposite to the behavior of superfluid transition of all known superfluids. Namely, the TO signals become larger when the excitation is smaller over decades of amplitude change. We discuss that it is fluctuation of the thermally excited quantized vortices in the VF state [1]. The VF state has been observed and heavily discussed in various new types of superconductors starting from the Cuprate superconductors. Evidence of quantized vortices has been reported especially for Under-doped Cuprate superconductors [7]. The VF state in He is expected to become a 3D supersolid state at lower temperatures below some T_c, because of increase of low D coherence length towards lower T, which originates in lower dimensional subsystems in the system and causes a transition to a SS state with macroscopic coherence.

We have experimentally found a transition from the VF state to the SS state by observing a hysteresis in the TO response with changing excitation below a temperature, T_c [2]. Figure 1 shows the T dependence of both NLRS of VF and the hysteretic component of NLRS, which we argue to be associated with supersolid density ρ_s. Both are plotted as functions of T. This observation is consistent with our preliminary results of TO measurements under DC rotation, where the evidence of vortex lines penetration occurs below the same $T_c \sim 75$ mK, far below T_o.

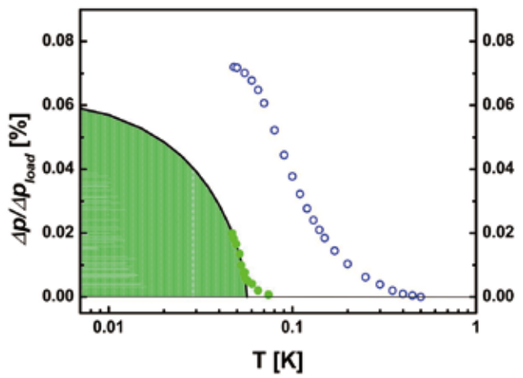

Fig. 1. "Non Linear Rotational Susceptibility(NLRS)" of the vortex fluid state (open symbols) and the hysteretic component of NLRS, $\Delta NLRS_{hys}$ (filled symbols) which we discuss to be supersolid density ρ_s, as a function of T. The high temperature part of NLRS behaves as $1/T^2$, whereas ρ_s starts from T_c and increases towards T = 0K and the latter behaves as an order parameter whereas NLRS does not behave as an order parameter. The NLRS of VF is found to behave as "paramagnetic", with Langevin function with $x \propto 1/T^2$. Langevin function behavior is expected for susceptibility of an ensemble of classical dipoles, but usually with $x \propto 1/T$.

References
[1] A. Penzev, Y. Yasuta, and M. Kubota, Phys. Rev. Lett. **101,** 065301 (2008).
[2] N. Shimizu, Y. Yasuta, and M. Kubota, arXiv:0903.1326., submitted to Phys. Rev. Lett.
[3] see a review, for example, D. Galli and L. Reatto, J. Phys. Soc. Jpn. **77**, (2008) 111010.
[4] E. Kim and M. H. W. Chan, Nature **427** 225 (2004).
[5] E. Kim and M. H. W. Chan, Science **305** 1941 (2004).
[6] P. W. Anderson, Nat. Phys. **3** 160 (2007); Phys. Rev. Lett. **100** 215301 (2008).
[7] Y. Wang, L. Li, M. J. Naughton, G. D. Gu, S. Uchida, and N. P. Ong, Phys. Rev. Lett. **95**, 247002 (2005).

Authors
N. Shimizu, A. Penzev, Y. Yasuta, and M. Kubota

Negative Interlayer Magnetoresistance and Three-Dimensional Dirac Holes in Bulk Graphite

Osada Group

We have newly found remarkable negative interlayer magnetoresistance (MR) in bulk graphite, which is considered to originate from the three-dimensional (3D) Dirac fermion nature of holes.

So far, many experimental studies have been performed on MR in bulk graphite. However, there has been no clear report on negative interlayer MR. In graphite, in-plane transverse MR is so huge that the anisotropy between in-plane resistance and interlayer one inverts under normal magnetic fields. Therefore, exact interlayer MR measurement is difficult because of the mixing of in-plane MR. In order to limit this mixing effect, we have prepared Kish graphite samples with flat surfaces and clear edge sides. Figure 1 shows the typical trace of interlayer MR observed in well-prepared graphite under normal magnetic fields. We can see the remarkable negative MR, on which clear Shubnikov-de Haas oscillations are superposed.

The negative MR observed in graphite is reminiscent of that observed in a layered organic conductor α-(BEDT-TTF)$_2$I$_3$ [1]. Recently, we theoretically showed that the multilayer Dirac electron system, where each layer has two-dimensional (2D) Dirac cone dispersion, shows negative interlayer MR [2]. Under magnetic fields, because of its massless nature, the Dirac electron system can easily reach the quantum limit where only the n = 0 Landau level (zero-mode) always exists at the Dirac point. The increase of zero-mode degeneracy causes strong negative MR. This

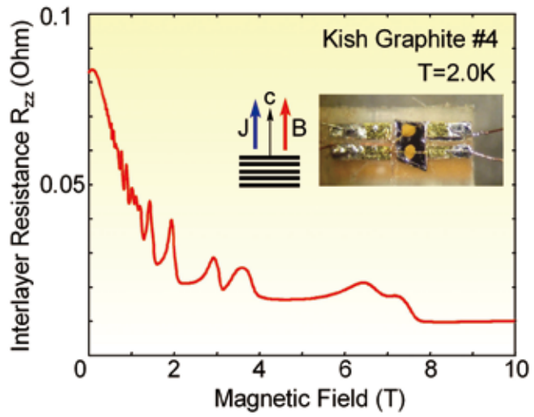

Fig. 1. Negative interlayer magnetoresistance observed in well-prepared bulk graphite.

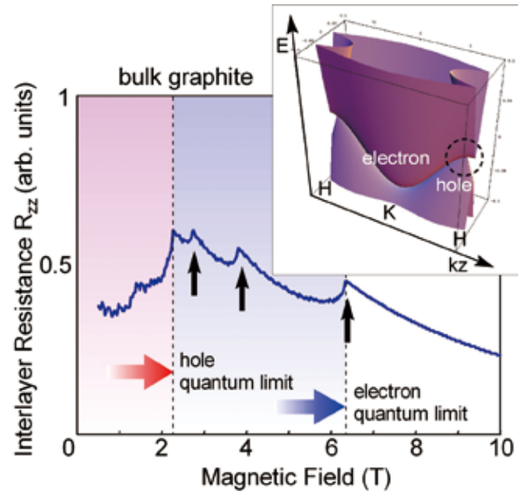

Fig. 2. Calculated interlayer magnetoresistance in bulk graphite. Inset shows the band dispersion along the H-K-H edge of the Brillouin zone. The broken circle indicate the Dirac-cone of holes.

picture strongly suggested the fact that α-(BEDT-TTF)$_2$I$_3$ has a Dirac-cone dispersion. In the case of bulk graphite, however, we cannot simply apply our theory, since the negative MR of graphite appears even in magnetic fields lower than the quantum limit where the zero-mode conduction is dominant.

Although monolayer graphite (graphene) has 2D Dirac-cone dispersion, bulk graphite is not a simple multilayer Dirac electron system because of its alternative stacking. In its 3D band dispersion, however, there exists the 3D Dirac-cone dispersion around the H-point in **k**-space. As a result, H-point holes show Dirac fermion nature whereas K-point electrons are conventional fermions. So, H-point holes reach the quantum limit at the much lower magnetic field than K-point electrons. Therefore, in graphite, negative MR could be expected in the wide field region corresponding to the quantum limit of holes. In fact, negative MR accompanied by Shubnikov-de Haas oscillations of electrons has been successfully reproduced by the calculation of Landau subband conduction employing the Slonczewski-Weiss-McClure band model as indicated in Fig. 2.

References
[1] N. Tajima *et al*., cond-mat 0812.0857.
[2] T. Osada, J. Phys. Soc. Jpn. **77**, 084711 (2008).

Authors
T. Osada, H. Imamura, K. Uchida, S. Sugawara, and T. Konoike

Intrinsic Properties of $SrFe_2As_2$ Single Crystal under Highly Hydrostatic Pressure Conditions

Uwatoko Group

The recent discoveries of superconductivity (SC) on iron-pnictide compounds have attracted much attention in the field of condensed matter physics. The parent compounds containing FeAs layers exhibit structural and magnetic phase transitions associated with Fe moments. Chemical substitution and applying pressure suppress the AF transition, resulting in the appearance of SC. An important clue in regard to the mechanism of SC should be provided by high pressure experiment on a stoichiometric sample since the application of pressure does not introduce disorder. However, fundamental problems remain to be solved, as the appearance of the pressure-induced SC is highly sensitive to pressure homogeneity. Furthermore, there is no bulk evidence for the SC transition since most of previous reports are carried out by resistivity measurement due to the experimental difficulty of high pressure experiment. To resolve these problems, we measured electrical resistivity and ac magnetic susceptibility of $SrFe_2As_2$ single crystals under highly hydrostatic pressure conditions up to 8 GPa.

Figure 1 shows the temperature dependence of the real part of χ_{ac} under pressure, relative to that of normal state. At 3.0 GPa, there is no apparent change in χ'. With increasing pressure, a noticeable drop appears close to the temperature T_{SC} obtained by aforementioned resistivity measurements, although the SC diamagnetism at 5.0 GPa is around 60 % with a broad transition width, implying the presence of the normal state portion in the sample. When the pressure is raised up to 5.5 GPa, the transition becomes sharper, and the nearly perfect shielding was detected. This result indicates

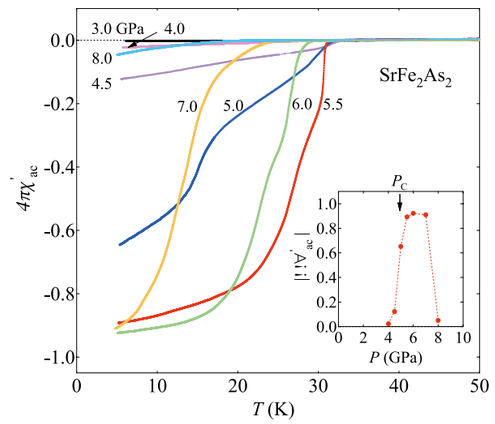

Fig. 1. Temperature dependence of the real part of ac magnetic susceptibility χ_{ac} for $SrFe_2As_2$ single crystal under pressure, relative to that of normal state. Inset shows the pressure dependence of the SC volume fraction $|4\pi\chi'|$.

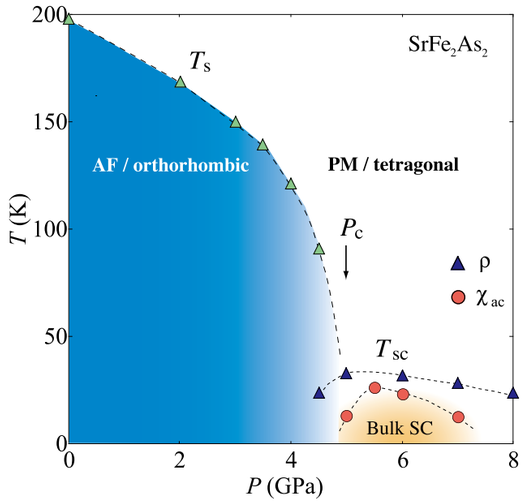

Fig. 2. Temperature-pressure phase diagram of $SrFe_2As_2$. Filled triangles and circles are determined from resistivity and ac susceptibility, respectively. The SC transition temperature T_{SC} is defined as a temperature of zero resistance and 50% of the full shielding effect. Broken lines are guides for the eye.

that the SC transition is a bulk origin. Interestingly, the transition begins to broaden again at higher pressures, and thus shielding effect becomes abruptly weak at 8.0 GPa. To show the pressure dependence of the SC volume fraction, we plot the magnitude of $4\pi\chi$' at the lowest temperature studied here (see the inset of Fig. 1). $|4\pi\chi'|$ remarkably increases above 5.0 GPa, exhibiting a value (~1) corresponding to the full shielding effect in a narrow pressure region. Note that this pressure almost coincides with the P_C where the AF and structural transitions at T_S disappear. In Fig. 2, we summarize T_S and T_{SC} obtained from our high pressure experiments to construct a temperature-pressure phase diagram of $SrFe_2As_2$. As the external pressure increases, T_S starts to decrease steeply above 3.5 GPa, and then seems to be suppressed to zero in the vicinity of P_C ~ 5.0 GPa. At 4.5 GPa, we observed the resistivity anomaly both due to antiferromagnetic and superconducting (zero resistance) transitions, suggesting the coexistence of AF and SC. Indeed, the onset temperature of the shielding effect approximately corresponds to the zero resistance temperature, but SC volume fraction is quite small. Since zero resistance due to SC transition can occur with a tiny volume fraction, the inhomogeneity of the pressure distribution leads to the deviation from the ideal phase diagram. Therefore, bulk SC only appears above P_C, where T_S is fully suppressed. This is consistent with the rapid sharpening of the SC transition width and remarkable increase of SC volume fraction exceeding P_C. Consequently, we suggest that the SC does not coexist with the AF/orthorhombic phase. We conjecture that the lattice/magnetic instability in the vicinity of P_C plays a crucial role in the appearance of the SC.

Authors
K. Matsubayashi, N. Katayama[a], K. Ohgushi, A. Yamada[b], K. Munakata, T. Matsumoto, and Y. Uwatoko
[a]University of Virginia
[b]Saitama University

Exciton-Biexciton-Plasma Crossover and Optical Gain in Quantum Wires

Akiyama Group

Roles of electron-hole (e-h) plasmas, biexcitons, and excitons in formation of optical gain as well as underlying physics of exciton Mott transition or crossover have attracted great interests in optical study of semiconductors. We have investigated these problems by developing high-quality T-shaped GaAs quantum-wire lasers fabricated by cleaved-edge overgrowth with molecular beam epitaxy [1-4].

Simultaneously measured excitation-power-dependent photoluminescence (PL) and gain/absorption spectra of a

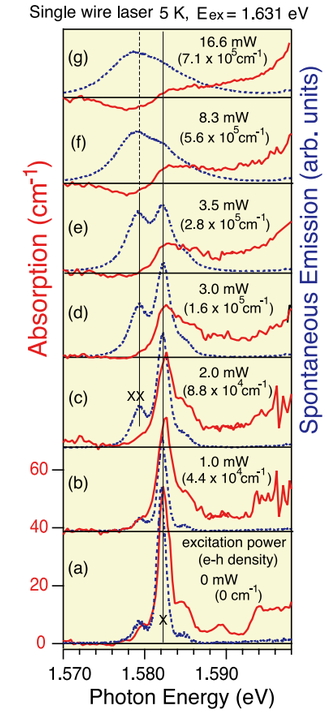

Fig. 1. Absorption (solid curves) and PL (dashed curves) spectra from a single T-wire at 5K for various excitation powers (densities) from (a) nearly zero to (g) 16.6 mW (7.1 × 10^5 cm^{-1}). All data were measured for uniform excitation except for the absorption in (a). The vertical lines indicate the energies of the biexciton (XX) and exciton (X) PL peaks.

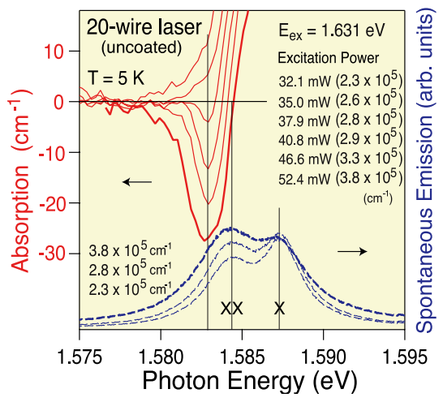

Fig. 2. Absorption spectra (solid curves) and PL (dashed curves) spectra of a 20-wire laser for various e-h densities.

single-wire laser (Fig. 1) and of a 20-wire laser (Fig. 2) were obtained. They showed that clear exciton (X) and biexciton (XX) peaks were still visible in the PL when the exciton peak was bleached from the absorption spectrum, and also that optical gain appeared in the absorption spectrum when the XX biexciton emission overtook the X exciton emission. This indicated that biexciton-exciton population inversion led to sharp optical gain before the Mott transition in a 1D system. As the gain grew and broadened without a peak shift, the exciton PL was quenched and broad plasma PL evolved from biexciton PL, indicating a continuous change in gain mechanism from biexcitons to an unbound e-h plasma. Our results demonstrated that the Mott transition from excitons to plasma occurs via biexcitons, and optical gain does not always signify the Mott transition of excitons. Biexcitons play key roles in optical spectra in the exciton-plasma cross-over or the exciton Mott transition.

References

[1] Y. Hayamizu *et al.*, Phys. Rev. Lett. **99**, 167403 (2007).
[2] M. Yoshita *et al.*, Phys. Rev. B **74**, 165332 (2006).
[3] T. Ihara *et al.*, Phys. Rev. Lett. **99**, 126803 (2007).
[4] H. Akiyama *et al.*, Physica E **40**, 1726 (2008).

Authors

H. Akiyama, M. Yoshita, Y. Hayamizu, T. Ihara, L. Pfeiffer[a], K. West[a], P. Huai[b], K. Asano[c], T. Ogawa[c], and C. Z. Ning[d]
[a]Bell Laboratories, Alcatel Lucent
[b]Shanghai Institute of Applied Physics
[c]Osaka University
[d]Arizona State University

Nanoscale Chemical Imaging by Scanning Tunneling Microscopy Assisted by Synchrotron Radiation

Synchrotron Radiation Laboratory and Hasegawa Group

The microscopy having the spatial resolution of atomic scale with the function of element specificity is one of the ultimate microscopy for materials science. To this end, we have developed scanning tunneling microscopy (STM) system assisted by a core-level electron excitation by synchrotron radiation light (SR) [1]. Recently, we have reported the possibility of the element-specific imaging by the SR assisted STM (SR-STM) and a quite high-spatial resolution (~ few tens nm) has been demonstrated [2]. Here, we present some more evidences of the capability of the element-specific STM observation in high-spatial resolution by the SR-STM.

The experiment was done on the beamline BL-13C at Photon Factory, KEK. As a test sample, checkerboard patterned sample consisting of Fe and Ni stripes with the thickness of about 5 and 10 nm was fabricated on a Au thick film formed on Si(100) substrate by an electron beam lithography. The width of the stripes is 1μm each. Because of the sequence of the stripe formations (Fe after Ni), Fe stripes are located at the top of the sample surface and covers partially the Ni stripes as illustrated in Fig. 1(a). The detailed setting of the SR-STM measurement is presented elsewhere [2].

In order to obtain the element specific images, we performed the STM observation during irradiating the sample surface with the SR light of different photon energies at around Fe and Ni *L* absorption edges. Figure 1(b) is a topographic image of the sample taken in the constant current mode by the SR-STM. We can see the checkerboard pattern clearly. Figures 1(c) and (d) represent the photo-induced current images taken simultaneously with the topographic image at the top of Fe L_3 ($h\nu$ = 706 eV) and Ni L_3 ($h\nu$ = 852 eV) edges, respectively by using lock-in technique [2]. As shown in the figures, the photo-induced current causes significant contrast that depends on the element of the stripe structures. That is, the area of Fe is the brightest and that of Ni is the darkest in Fig.1(c) and (d). However, the photo-induced current image does not depend much on the exciting photon energies. The observed almost unchanged contrast is probably caused by the work-function difference of the materials. It has been reported that the Fe has much smaller work-function than that of Ni [3]. Since in the SR-STM measurement observed photo-induced current is dominantly due to secondary electrons which are inelastically scattered after excited by incident photons, the intensity of photo-induced current is inversely proportional to work-function and proportional to ionization cross section. The ionization cross section is nearly the same between Fe and Ni because the both two elements are neighbor in the periodic table, and the difference in photo-induced current by the work-function difference may cause the contrast.

In order to reduce the strong contrast that is not sensitive to the photon energy and to enhance the photon energy dependence, we have divided the photo-induced current image taken at the absorption edge-top by that of at the edge-bottom. Figures 1(e) and (f) are the images obtained by this procedure. In Fig.1(e), the photo-induced current image at $h\nu$ = 706 eV (= edge top) has been divided by that taken at $h\nu$ = 698 eV (= edge bottom). Now, as shown in Fig. 1(e), the region of Fe has larger intensity than that of Ni. Interestingly, the contrast has been inverted if we divide the images

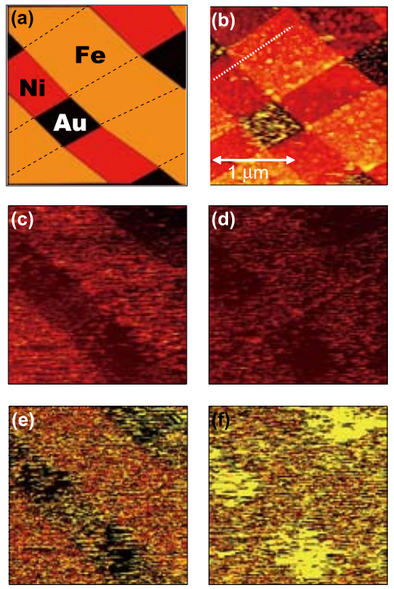

Fig. 1. Images of an Fe and Ni checkerboard pattern observed by SR-STM with (b) constant current mode (topographic image), (c) photo-induced current image at $h\nu$ = 706 eV and (d) 852 eV. Schematic illustration is presented in (a). Elemental specific image of Fe is presented in (e) that is obtained by dividing photo-induced current image at Fe *L* absorption edge top ($h\nu$ = 706 eV) by that taken at edge bottom (698 eV). (f) the same as (e) but obtained with images at the Ni *L* absorption edge ($h\nu$ = 852 /843 eV) .

taken at the Ni absorption edge-top ($h\nu$ = 852 eV) by that of the edge-bottom ($h\nu$ = 843 eV) as in Fig. 1(f). This contrast inversion between the Fe and Ni absorption edges indicates that one can obtain element specific images by SR-STM by utilizing the energy tunability of synchrotron radiation.

The spatial resolution of the photo-current image can be roughly estimated by taking the intensity line profile in Fig. 1(c) along the dotted line indicated in Fig. 1(b). From the line profile (not shown here) the resolution of about 30 nm is obtained. Considering the intrinsic edge width of the patterned sample (~ 20 nm) the real spatial resolution of photo-current signal can be estimated as about 10 nm [4]. The obtained value is comparable to or even better than the best spatial resolution of photoemission electron microscopy observation.

Although the mechanism of achieving such a high spatial resolution is still not clear, the local detection of the photo-induced secondary electrons through the surface barrier lowered by the proximate tip and/or via the tunneling process probably plays an important role.

References

[1] T. Matsushima *et al.*, Rev. Sci. Instrum. **75**, 2149 (2004).
[2] T. Eguchi *et al.*, Appl. Phys. Lett. **89**, 243119 (2006).
[3] D. E. Eastman, Phys. Rev. B **2**, 1 (1970).
[4] T. Okuda *et al.*, Phys. Rev. Lett. **102**, 105503 (2009).

Authors

T. Okuda, T. Eguchi, K. Akiyama[a], A. Harasawa, T. Kinoshita[b], Y. Hasegawa, M. Kawamori[c], Y. Haruyama[c], and S. Matsui[c]
[a]Tohoku University
[b]SPring-8, JASRI
[c]University of Hyogo

Development of a Phase Shifter with Laminated Permalloy Yokes for Multi-Segment Undulators

Nakamura Group

A phase shifter is used to control the radiation phase between two undulator segments by giving a bump orbit to an electron beam with its magnetic field and can be applied to novel undulators such as a polarization-controlled undulator [1,2] and very long undulators in synchrotron radiation(SR) sources and FELs that have to consist of undulator segments separated by finite distances. The phase shifter generally has to make a phase shift of 0 to 2π or more for all the wavelengths. High stability and reproducibility of the phase control is required to avoid orbit movements of the electron beam and quality degradation of the SR beam. Furthermore fast control of SR wavelength and polarization including helicity switching is often needed for the phase shifter.

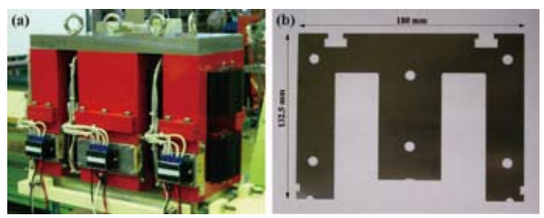

Fig. 1. (a) Phase shifter prototype and (b) 0.1-mm-thick permalloy lamination used for the yokes.

We designed and fabricated a phase shifter prototype with 0.1-mm-thick permalloy laminations to satisfy the requirements for the phase shifter. The phase shifter prototype consists of three H-type dipole magnets (Magnet A, B and C) with the yoke-length ratio of 1:2:1. Each magnet has a yoke divided into two parts at the horizontal symmetric plane and two coils for the upper and lower magnetic poles. Figure 1(a) shows the fabricated phase shifter prototype. Each half yoke is made of 0.1-mm-thick permalloy laminations united and insulated by varnish. Figure 1(b) shows a permalloy lamination used for the yokes. All the permalloy laminations are formed by stamping and annealed at about 1100 °C to maximize their magnetic permeability. We succeeded in reducing the size error of the laminations down to ±0.1 mm even after annealing. They have a very high magnetic permeability (about 400000) and very low hysteresis. The three magnets are independently excited by three identical power supplies, which are linear amplifier type and developed so that it should have good frequency response and low ripple and drift less than 100 ppm (10^{-4}) of the maximum current.

Field measurements were performed using a 3-D field measurement system with a Hall probe and a 3-D movable

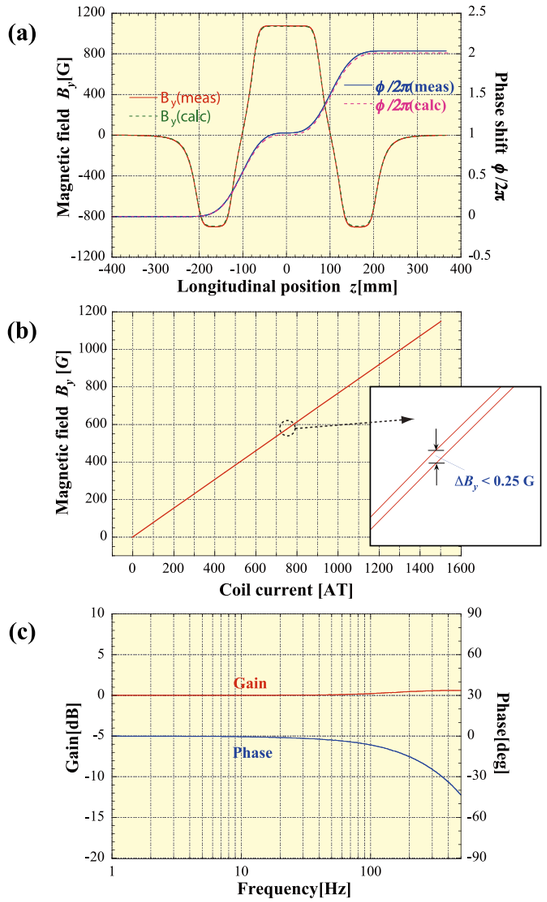

Fig. 2. Field measurement results: (a) measured longitudinal field distribution and phase shift expected from the distribution with the 3-D field calculation result, (b) excitation curve of Magnet B and its ultra-low hysteresis and (c) frequency response of Magnet A up to 500 Hz.

stage. Figure 2(a) shows the measured longitudinal field distribution and the phase shift due to the field distributions at coil currents of $I_A = I_C = -1170$ AT and $I_B = 1400$ AT. The measurement result is in good agreement with the result of 3-D magnetic field calculation. The maximum phase shift given by this prototype is about 4π for an assumed maximum radiation wavelength of $\lambda = 4.959$ nm (250 eV). Figure 2(b) shows the excitation curve of Magnet B and its hysteresis effect. The excitation curve is almost linear and the magnetic field is not saturated up to the maximum coil current of 1500 AT. Due to the ultra-low hysteresis of the yoke, the hysteresis effect was only 0.25 G at maximum. Figure 2(c) shows measured frequency response of Magnet A. The gain was kept constant within 1 dB up to 500 Hz and the phase delay was less than 1 degree at 10Hz and 10 degrees at 100 Hz. The phase shifter prototype with laminated permalloy yokes showed good performance in reproducibility and frequency response of the magnetic field.

References

[1] M. Oshima and A. Kakizaki, Journal of JSSRR **20** No. 6, 383 (2007).

[2] T. Tanaka and H. Kitamura, AIP Conference Proceedings **705**, 231(2004).

Authors

N. Nakamura, K. Shinoe, I. Ito, T. Shibuya, A. Ishii, H. Kudo, H. Takaki, H. Tanaka[a], H. Kitamura[a], and T. Bizen[b]

[a]RIKEN SPring-8,

[b]JASRI/SPring-8

High-Strength Hydrogel with Ideally Homogeneous Network Structure

Shibayama Group

Hydrogels are defined as 3 dimensional polymer networks, in which the polymer chain networks are highly immersed by water and the water content is typically over 90%. By taking advantage of their high water absorption and

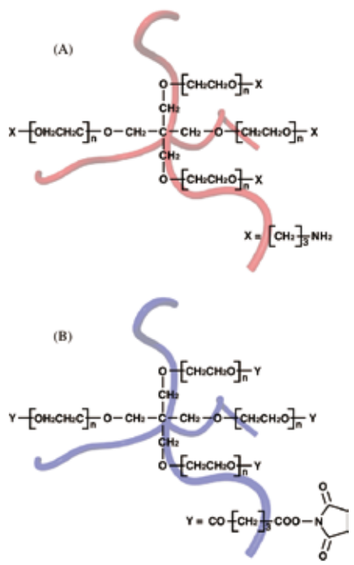

Fig. 1. Molecular structures of TAPEG (a) and TNPEG (b).

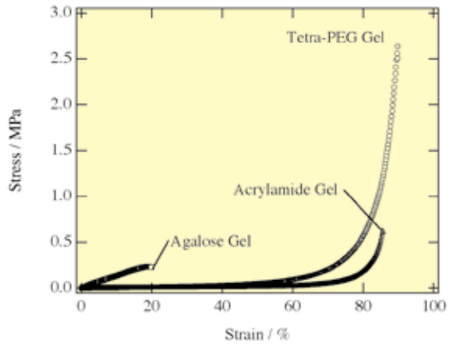

Fig. 2. Stress-Strain curves of agarose gel (square), acrylamide gel (triangle), and Tetra-PEG gel (circle).

retention properties, hydrogels have been applied to diapers, contact lenses, drug reservoirs, etc. Despite these practical applications, applications of hydrogels to structural materials are restricted because of their poor mechanical properties, which result from the micro-inhomogeneities created by cross-linking reactions. Here, we show the new strategy for forming a homogeneous network by decreasing the degree of freedom of the micro-network structure.

We successfully designed and fabricated a novel homogeneous hydrogel by combining two symmetrical tetrahedron-like macromers (the building blocks) of the same size. The macromers are tetra-amine terminated PEG (TAPEG) and Tetra-NHS-glutarate terminated PEG (TNPEG). Here, NHS represents for *N*-hydroxysuccinimide. These are prepared from tetra-poly(hydroxylpolyethylene glycol)s which were synthesized by successive anionic polymerization reaction of ethylene oxide from sodium alkoxide of pentaerythritol. We formed the gel by combining two well-defined symmetrical tetrahedron-like macromers of the same size (Figure 1). We call these gels Tetra-PEG gels. Since each macromer has four end-linking groups reacting each other, these two building units must connect alternately without self-binding reaction. Both TAPEG and TNPEG macromers and the reaction itself are biocompatible, and the compressive strength of thus prepared Tetra-PEG gels was in a MPa-range which was much superior to those of agarose gels or acrylamide gels having the same network concentrations (Figure 2). It is already confirmed that the mechanical strength reaches 30 MPa by tuning the molecular weight and concentrations, which is three times as high as that of native articular cartilage (≈ 10MPa).

Small-angle neutron scattering studies on Tetra-PEGs having various molecular weights revealed that Tetra-PEG gels form a tetrapod-like structure with extremely low degrees of defects (Figure 3). This is the reason of the

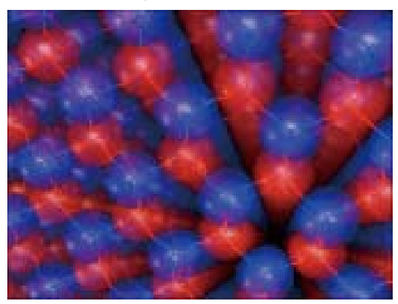

Fig. 3. Schematic illustration of a model structure for Tetra-PEG gel. Red and blue spheres represent TAPEG and TNPEG, respectively.

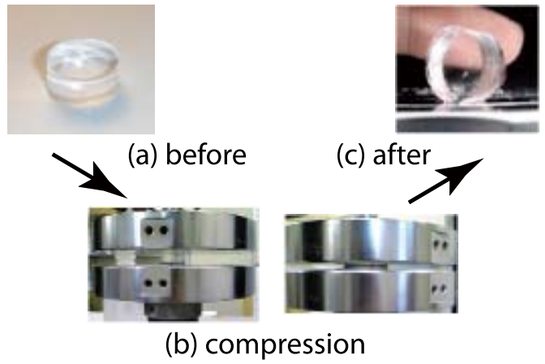

Fig. 4. (a) Photograph of Tetra-PEG gel (a) before, (b) during, and (c) after compression test.

extraordinarily good mechanical properties of gels. Hence, Tetra-PEG gel may be valuable in application for practical use. In the case of biomedical applications, hydrogels are required to meet three criteria at the same time: high-mechanical properties, biocompatibility and an easy fabrication process. A Tetra-PEG gel satisfy all three criteria. First, it has attained high-mechanical properties using symmetrical tetrahedron-like constitutional polymers to form an extremely homogeneous structure (Figure 4). Second, Tetra-PEG gel uses biocompatible tetrahedron-like PEG with mutually reactive terminal groups; its gel formation reaction does not use or produce any toxic substance. Third, Tetra-PEG gel can be fabricated within a few minutes through *in situ* gelation by simply mixing two macromer solutions. Because of these combined merits, we strongly believe that Tetra-PEG gel and its derivatives may be useful in the biomedical field.

References

[1] T. Sakai, T. Matsunaga, Y. Yamamoto, C. Ito, R. Yoshida, S. Suzuki, N. Sasaki, M. Shibayama, U. Chung, Macromolecules **41**, 5739 (2008).

[2] T. Matsunaga, T. Sakai, T. Y. Yamamoto, Y. Akagi, U. Chung, M. Shibayama, Macromolecules **42**, 1344 (2009).

Authors

T . Sakai, T . Matsunaga, Y. Yamamoto, C. Ito, R. Yoshida, S. Suzuki, N. Sasaki, Y. Akagi, U. Chung, and M. Shibayama

Short- and Intermediate-range Structure and Slow Dynamics of an Ionic Liquid C8mimCl

Yamamuro Group

Ionic liquids (ILs) are very interesting materials not only for various applications but also for basic science of liquids. Most of ILs have glass transitions at low temperatures and the related temperature dependence of viscosity is not understood by Stokes-Einstein scenario. This can be related to hierarchical structure and dynamics of ILs. Most of cations of ILs have core parts with positive charge and also have mostly neutral methyl-groups and longer alkyl-chains. Furthermore, it was recently found that ILs have separating ionic and neutral (alkyl-chain) domains of a nanometer scale. They may have different time scales of diffusive motions. The purpose of our study is to clarify the hierarchical structure and dynamics of ILs by using various neutron scattering techniques, *i.e.*, neutron diffraction, quasi- and inelastic scattering, spin echo, etc. We have already investigated several imidazolium ILs with relatively shorter alkyl-chains and found that alkyl-chains are highly disordered and moving very fast (in ps order) at room temperature. In this work, we have taken fully-deuterated 1-octyl-3-methy-imidazolium chloride (d-C8mimCl) which has relatively longer alkyl-chains and so may have clear domain structure. The deuteration was required to avoid strong incoherent scattering from hydrogen (H) atoms.

Figure 1 shows the neutron diffraction patterns of d-C8mimCl measured by HERMES (IMR, Tohoku Univ.) installed at JRR-3, JAEA. The peaks around 0.3, 1.1, and 1.4 $Å^{-1}$ are considered to be due to the correlations of domains, ions, and alkyl-chains, respectively. As cooling the sample, the inter-ionic and inter alkyl peaks shifted to the high-Q side, indicating compact packing of local structure, while the inter-domain peak was grown and shifted to the low-Q side, indicating clear contrast and expansion of domains. The diffraction pattern was not changed much around 190 K because of the freezing phenomenon (glass transition) around 200 K. This is the first neutron diffraction data demonstrating clear temperature dependence of IL domains. Figure 2 shows the intermediate scattering function of d-C8mimCl obtained by a neutron spin-echo (NSE) instrument installed at National Institute of Standard and Technology (NIST), USA. There were fast and slow relaxations depending on temperature. These curves were fitted well with the combination of an exponential and a stretched exponential functions as shown in Fig. 2. The fast motion did not change much with temperature while the slow motion had Arrhenius temperature dependence with the activation

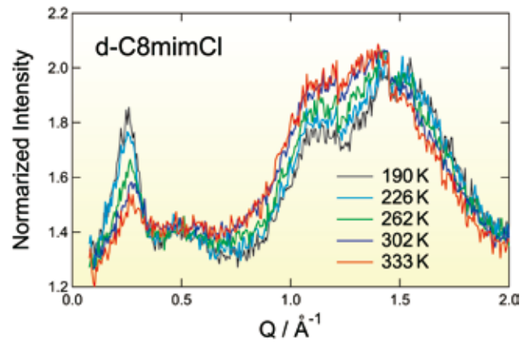

Fig. 1. Neutron diffraction patterns of d-C8mimCl ionic liquid measured as a function of temperature.

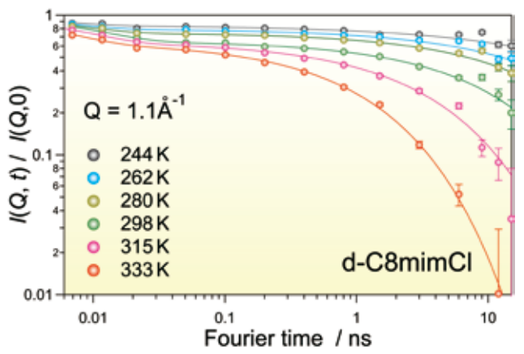

Fig. 2. Intermediate scattering function of d-C8mimCl ionic liquid measured by a neutron spin echo technique as a function of temperature.

energy of 36 kJ mol^{-1}. The fast and slow motions may be related to the local motion of alkyl-chain and the diffusion of ions, respectively. The time-scale of domain motion was found to be slower than 10 ns from the NSE measurement at Q = 0.28 Å^{-1}. This is also the first data showing the dynamics of ions and domains of ILs.

Authors
O. Yamamuro, T. Yamada, and M. Nagao[a]
[a]NIST and Indiana University

Single-crystal Neutron-Inelastic-Scattering Study on $BaFe_2As_2$; a Parent Compound for the Fe-Based Superconductors

Sato Group

Discovery of the high-T_c superconductivity in Fe-based compounds in early 2008 generated a tremendous boom in the solid-state-physics community. One of the central issues for understanding the mechanism of the high-T_c superconductivity in the Fe-based compounds is role of Fe spin fluctuations. Shortly after the discovery, it was suggested that the Fe moments originate from itinerant 3*d* electrons. Indeed, the parent (non-superconducting) compounds are poor metals with spin-density-wave (SDW) type antiferromagnetic ordering accompanied by structural transitions in common. This itinerant magnetism is in striking contrast to the Mott-insulator-type localized magnetism in parent compounds of the cuprates, the highest-T_c superconductors ever found. It is, therefore, of enormous importance to elucidate how the itinerant Fe moments fluctuate both in the SDW phase of the parent compound and in the superconducting phase of the doped systems. To reveal the spin fluctuation spectrum, we, therefore, performed neutron inelastic scattering study on the parent compound $BaFe_2As_2$ using single-crystalline sample.

Figure 1 shows the single-crystalline sample, which was grown using the vertical Bridgman technique in the present study. The crystals with total mass of about 0.4 grams were co-aligned and used in the inelastic neutron scattering study, performed using the thermal and cold-neutron triple-axis spectrometers ISSP-GPTAS and HER, installed at JRR-3, Tokai, Japan.

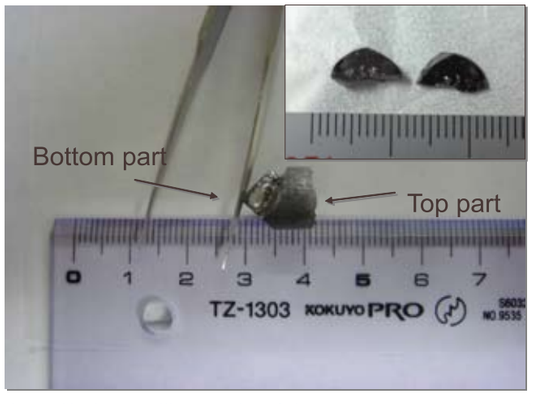

Fig. 1. Single crystalline samples of the $BaFe_2As_2$ parent compound grown by the Bridgman technique. At the bottom part, single grains were grown. Inset: the crystals removed from the Bridgman ingot.

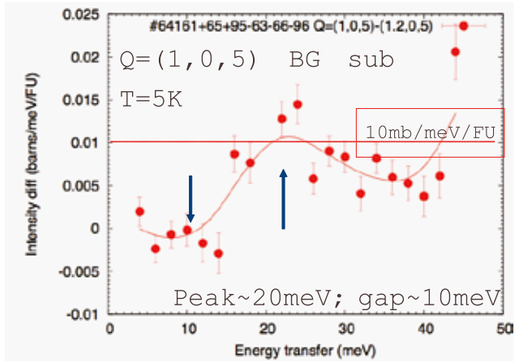

Fig. 2. Neutron inelastic scattering spectrum at the antiferromagnetic zone center Q = (1,0,5) and at T = 5K.

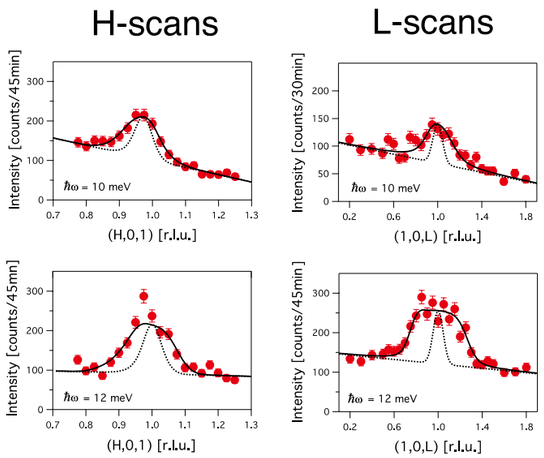

Fig. 3. Constant-E scans around the antiferromagnetic zone center Q = (1,0,1) in the in-plane and out-of-plane directions.

Figure 2 shows the low-energy spin excitations in the parent compound, measured at the antiferromagnetic zone center Q = (1,0,5) at the base temperature. We note that we used the low-temperature orthorhombic coordinate in this report. Apparently, an inelastic intensity starts to increase above $\hbar\omega$ = 9.5 meV, and peaks around $\hbar\omega$ = 20 meV. The Q-dependence of the inelastic intensity is shown in Fig. 3. It peaks at the antiferromangetic zone center at low energies, whereas the peak starts to broaden at higher energies. Detailed analysis shows that the inelastic peak corresponds to the spin-wave-like excitations with very steep in-plane and relatively weak out-of-plane dispersions. It should be noted that the ratio of the spin-wave velocities for the in-plane and out-of-plane dispersions is quite large as 0.2, which is very different from that in the high-T_c cuprates. In gh-energy regions above 20 meV, we have observed appearance of highly 2D scattering independent of L in addition to the spin-wave excitations. We suggest that this may be electron-hole excitation continuum across the SDW gap. Further studies in higher energies as well as the Co-doped compounds are in progress.

Reference
[1] K. Matan, R. Morinaga, K. Iida, and T. J. Sato, Phys. Rev. B **74** 54526 (2009).

Authors
T. J. Sato, K. Matan, R. Morinaga, and K. Iida

Novel Devil's Staircase Transitions under Pressure

Y. Ueda Group

Among various vanadium bronzes, β-vanadium bronzes, which have mix-valence vanadium atoms, exhibit wide variety of attractive properties, such as charge orderings, metal-insulator transitions, and pressure-induced superconductivities [1]. In addition to these, we discovered novel type of phase transitions under pressure in the compound with Sr as a cation, which are strongly related to the symmetry of the crystal and the one-dimensional nature of the system. The compound has a monoclinic crystal structure with vanadium chains along the b-axis, and it is a quasi-one-dimensional system.

At ambient pressure, the Sr compound takes place a charge ordering transition at low temperature, accompanied by a formation of three-fold superlattice along the b-axis. By applying pressure, the charge order state with a tripled unit cell is suppressed, and another charge ordering state appears, which is well-distinguished in magnetic susceptibility data as shown in Fig. 1. X-ray diffraction study clarified that this new phase has five-fold superlattice. Also in the charge disorder phase, another phase was found in resistivity measurements. At least four phases are concentrated in a very narrow pressure and temperature region, suggesting competition among various states [2].

We conducted detailed structural investigations in this pressure and temperature region, and found many other phases with different periodicities along the b-axis as shown in Fig. 2. The observed periodicities are five, seven, and eleven, all of which are odd numbers including three observed under ambient pressure. All the observed phases are well-described by symmetry reduction from the crystal symmetry of the charge disorder phase. Strong couplings of charge ordering and crystal symmetry, restricts the periodicity to only odd numbers.

As an origin of the appearance of many phases with different periodicities, we propose a self-doping model between two types of vanadium chains. The system has two types of vanadium two-leg ladders. Suppose that all

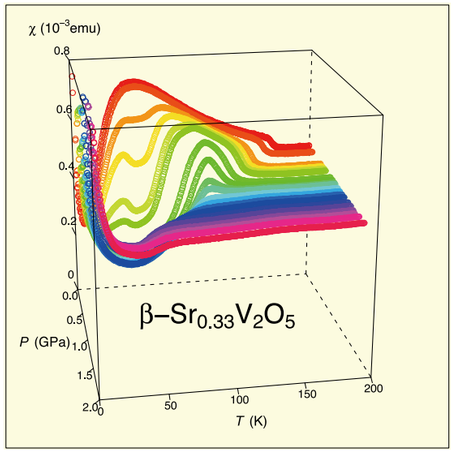

Fig. 1. Pressure dependence of of magnetic susceptibility. At ambient pressure, susceptibility exhibits Curie-Weiss behavior below the charge ordering temperature, and shows a spin-gap feature at low temperatures. By applying pressure, additional anomaly is observed in the charge order region, indicating appearance of a new charge order state.

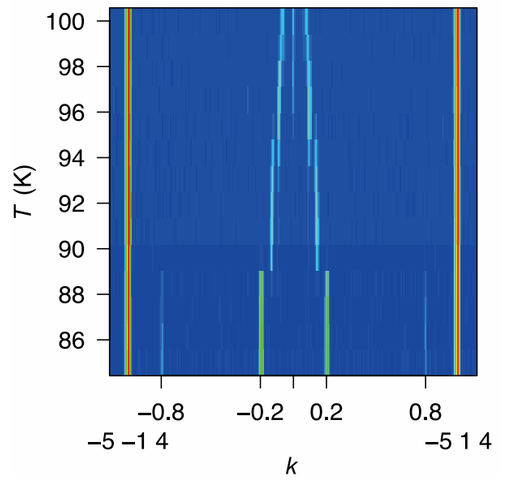

Fig. 2. Temperature dependence of x-ray diffraction intensity measured at 0.9 GPa. Superlattice signals indicate devil's staircase-type transitions. At low temperature, signals at 0.2 and 0.8 represent the five-fold supperlattice. By elevating temperature, the position of the superlattice signal moves stepwise to 1/7, 1/11, etc.

vanadium atom has the same charge, the occupancy is 1/3, which leads the periodicity three observed under ambient pressure. By application of pressure and/or change of temperature, charge could transfer between two types of ladders, and this varies the charge modulation, which generates many periodicities.

References
[1] T. Yamauchi and Y. Ueda, Phys. Rev. B **77**, 104529 (2008).
[2] T. Yamauchi, H. Ueda, J.-I. Yamaura, and Y. Ueda, Phys. Rev. B **75**, 014437 (2007).

Authors
H. Ueda, T. Yamauchi, Y. Ueda, K. Ohwada[a], and H. Sawa[b]
[a]JAEA, SPring-8
[b]Nagoya university

Incommensurate Order and Rotational-Symmetry Breaking in 2D Frustrated Heisenberg Model

Kawashima Group

The magnetic compound $NiGa_2S_4$ is a rare example of a two-dimensional triangular lattice antiferromagnet and stays in a spin-disordered state at low temperatures. Interesting behaviors of this material were observed by Nakatsuji group [1,2]. For example, development of incommensurate (IC) spin correlation was confirmed by magnetic neutron scattering experiment. It is easy to see that the incommensurate magentic ordering can be stabilized at least for zero-temperature by introducing a dominant antiferromagnetic third-nearest-neighbor interaction.

Introduction of such intermediate-range interaction may cause various effects in addition to the incommensurate ordering. To study the consequence in more depth, we investigate a two-dimensional classical Heisenberg model on a triangular lattice with a ferromagnetic nearest-neighbor (NN) interaction J_1 (<0) and an antiferromagnetic third-NN inter-

action J_3 (>0). The model Hamiltonian is given by

$$\mathcal{H} = J_1 \sum_{\langle i,j\rangle_{\mathrm{NN}}} \boldsymbol{s}_i \cdot \boldsymbol{s}_j + J_3 \sum_{\langle i,j\rangle_{\mathrm{3rd.NN}}} \boldsymbol{s}_i \cdot \boldsymbol{s}_j \qquad (1).$$

If the third-NN interaction is dominant, there are three equivalent IC ground-state spin-configurations that can be transformed to each other by 120 degree lattice rotations (Fig. 1). Presence of this discrete symmetry makes it possible to have a finite temperature phase transition without violating Mermin and Wagner's theorem.

We perform classical Monte Carlo simulation using the standard heat-bath method [3]. In this calculation, the value of the interaction ratio J_3/J_1 is fixed at *-3*. We find that the specific heat as a function of the temperature exhibits a single peak indicating a phase transition. We study the probability distribution of the energy in order to determine the order of this transition. The distribution exhibits the bimodal structure and the valley in the middle of the distribution deepens with increasing lattice size. These evidences clearly suggest the first-order phase transition.

From ground state properties of the present model, it is natural to expect the spontaneous breaking of the threefold lattice-rotational symmetry. Based on this expectation, we calculate the direction-specified nearest-neighbor correlation along the three axes separately. To be specific,

$$\varepsilon_\mu = \frac{1}{L^2} \sum_{\langle i,j\rangle_{\mathrm{NN}} \parallel \mathrm{axis}\,\mu} \boldsymbol{s}_i \cdot \boldsymbol{s}_j \quad (\mu = 1, 2, 3) \qquad (2).$$

In the symmetry breaking phase, one of the three ε_μ is negative, while the others are positive. We therefore sort the averages of the three quantities in descending order and define them as E_1, E_2, and E_3 . As shown in Fig. 2, E_1 and E_2 increase but E_3 decreases below the first-order phase transition temperature. The threefold symmetry is spontaneously broken and one of the three axes is selected.

We now consider implications of these results on the experimental observations of $NiGa_2S_4$. The important point there was that the IC phase emerges at low temperatures and the specific heat has a broad double-peak structure. The present results are consistent with the incommensurability observed in the neutron scattering experiments. On the other hand, however, the specific heat of the present model only exhibits a single divergent peak. To relate the present results to the experiment, it is necessary to construct the whole phase diagram and also take into account other types of interactions that have been neglected.

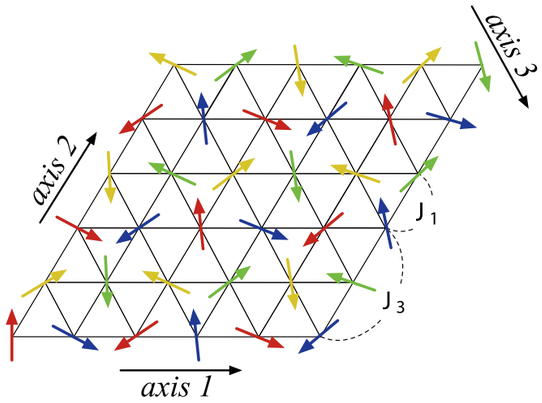

Fig. 1. A schematic illustration of spin configuration for the ground state. The spin configuration along axis 1 is characterized by the wave number k, and that of axes 2 and 3 by $k/2$. There is a threefold degeneracy corresponding to 120 degree lattice rotations. The spin configuration on each of the four sublattices (divided by color) is close to, but not exactly, the 120 degree structure.

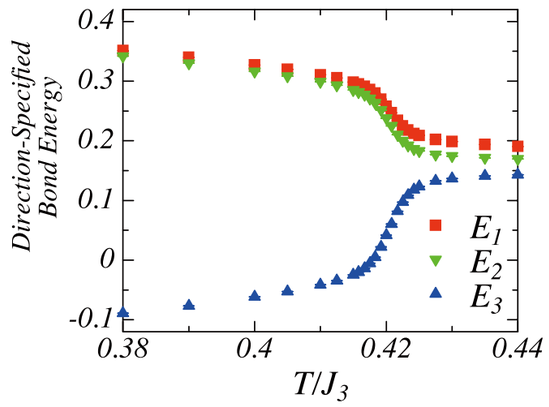

Fig. 2. Temperature dependence of the direction-specified bond energy E_1, E_2 and E_3. The first-order transition temperature is $T_c/J_3 \sim 0.42$.

References

[1] S. Nakatsuji, Y. Nambu, H. Tonomura, O. Sakai, S. Jonas, C. Broholm, H. Tsunetsugu, Y. Qiu, and Y. Maeno, Science **309**, 1697 (2005).
[2] Y. Nambu, S. Nakatsuji, and Y. Maeno, J. Phys. Soc. Jpn. **75**, 043711 (2006).
[3] R. Tamura and N. Kawashima, J. Phys. Soc. Jpn. **77**, 103002 (2008).

Authors
R.Tamura and N. Kawashima

Magnetic States of Highly Frustrated Spinel $ZnCr_2O_4$ under Ultra-high Magnetic Fields up to 400 T by Electro-Magnetic Flux Compression

Takeyama and Y. Ueda Groups

$ZnCr_2O_4$ is a geometrically frustrated antiferromagnet. Cr ions form a pyrochlore lattice in this material. The Néel temperature is 12 K while the Curie-Weiss temperature is such high as -390 K. This shows that a strong geometrical frustration prevents the Néel ordering. It is known that the lattice distortion accompanies the Néel ordering. Spin-lattice interactions act under the strong geometrical frustration in this material. As the exchange interactions between Cr ions are very strong, an ultra-high magnetic field is required to investigate the magnetization process of this material. We performed the Faraday rotation measurements under ultra-high magnetic fields up to 190 T by using a single turn coil [1]. We observed a first order phase transition at 120 T and a linear increase of Faraday rotation angle between 120 T and 135 T and the plateau with 1/2 of the full moment between 135 T and 160 T. These behaviors coincide with the theoretical prediction by K. Penc et al[2]. According to their theory, the region of the linear increase shows a cant 2:1:1 phase. In order to observe the full magnetization process of this material, a much higher field is required. We conducted the Faraday rotation measurements in magnetic fields up to 400 T by an electro-magnetic flux compression (EMFC) method. For a precise Faraday rotation measurement in the EMFC system, we have developed a hand-made optical cryostat fully made of a "stycast" resin (a picture above the figure), which enables us to achieve low temperatures with a fairly good vacuum tight. A curve in the figure shows the result. The left vertical axis shows the Faraday rotation angle (θ_F). The right vertical axis in the figure shows the magnetization which corresponds to the Faraday rotation angle. We successfully observed the full magnetization process of this material at 6 K. The data below 190 T coincides well with those measured by using the single turn coil. We found some anomalies which show new phase transitions (240 T, 290 T, 350 T, and 390 T) above 190 T. We considered that the anomaly at 390 T corresponds to the phase transition to the Ferro phase which is already explained in the theory by Penc *et al*. However, other phase transitions are beyond the prediction of the theory. The values of the magnetization at the fields of 240 T, 290 T and 350 T are 2/3, 3/4 and 5/6 of the full moment, respectively. The details of those phase transitions are still not clear. However, a possible explanation for these transitions is as follows. We assume that the 1/2 plateau phase has a rhombohedral spin structure (the inset of the figure). This structure shows that Kagome lattices with up-spins and triangular lattices with down-spins are alternately layered. If the spins in the triangular lattice layers form 1 up-2 down spin structures or 2 up-1 down structures in the high field region, new transitions can occur at 2/3 or 5/6 of the full moment. If such a structure is realized, it means that dimensional reduction of "magnetic ordering" takes place from three to two induced by an external strong magnetic field.

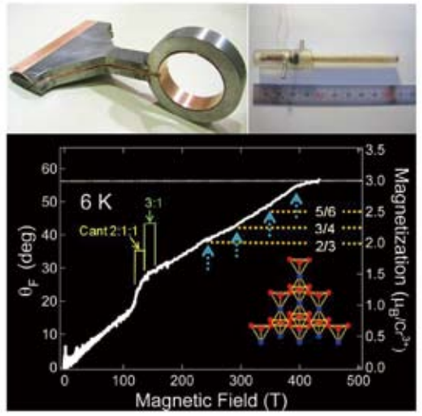

Fig. 1. Magnetization of $ZnCr_2O_4$ measured by the Faraday rotation method under ultra-high magnetic fields generated by the electro-magnetic flux compression method. Arrows show the phase transitions above the plateau phase. The upper left picture shows a primary coil for the electro-magnetic flux compression. The upper right picture shows a handmade optical cryostat made of a "stycast" resin.

References

[1] E. Kojima, *et al*., Phys. Rev. B **77** (2008) 212408.
[2] K. Penc *et al*., Phys. Rev. Lett. **93** 197203 (2004).; Y. Motome, *et al*., J. Mag. Magn. Mater. **300** 57 (2006).

Authors
E. Kojima, A. Miyata , S. Takeyama, H. Ueda, and Y. Ueda

Development of High-Speed Imaging System in Pulsed-Magnetic Fields

Tokunaga Group

The coupling between spin and lattice degrees of freedom realizes a variety of magnetic field-induced structural transitions. Recent development of diffraction measurements in pulsed-fields enabled us to obtain direct evidence of these phenomena for some materials in high-fields [1,2]. The accuracy, however, remains insufficient to detect faint changes caused by superstructures. Here, we developed an alternative technique to study these transitions: high-speed polarizing microscope imaging in pulsed-magnetic fields. Some kinds of structural transitions can be identified through observation of creation or annihilation of twin boundaries in crystals. With using a high-speed camera, we can perform this imaging in high magnetic fields achieved by pulse magnets. To this end, we introduced a high-speed camera (6000 frames/s for VGA resolution) on a commercial polarizing microscope. Using this microscope system and an objective lens with long working distance, we obtain real

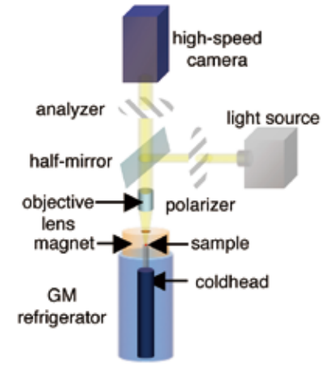

Fig. 1. Schematic drawing of the high-speed imaging system combined with a pulse magnet. The magnet and sample are cooled by the first and second stage of a cryocooler, respectively. The sample stage was mechanically isolated from the vibration of the compressor of the cryocooler and of the magnet. A high-speed camera is mounted on a commercial polarizing microscope to trace fast changes in images induced by pulsed-magnetic fields.

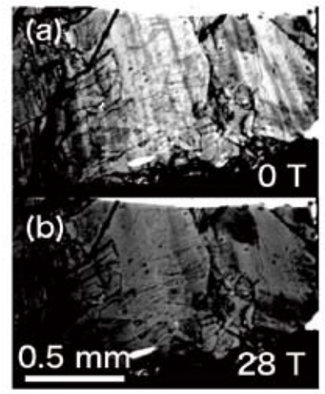

Fig. 2. Polarizing microscope images in the *ab*-plane of $La_{1/2}Sr_{3/2}MnO_4$ at 200 K at (a) zero field and (b) 28 T. The bright areas represent the domains of the COO, which disappear by application of a magnetic field of 28 T along the *c*-axis.

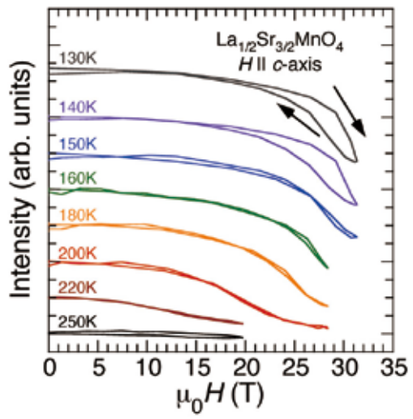

Fig. 3. Averaged intensity in a part of the polarizing microscope images as a function of the applied field. The data at each temperature is offset for clarity. The observed decrease in intensity corresponds the reduction in optical anisotropy caused by the COO.

images of samples located on the center of a small pulse magnet, which can generate magnetic fields up to 37 T in a duration time of about 5 ms. Using a low-vibration cryocooler system, the sample and the magnet can be cooled down to 8 K and 80 K, respectively.

As the first target of the present imaging system, we chose a crystal of $La_{1/2}Sr_{3/2}MnO_4$. This layered manganite exhibits charge/orbital ordering (COO) below about 220 K. Since the orbital ordering restricts the direction for hopping of mobile e_g electrons in the Mn^{3+} ions, optical anisotropy emerges within the *ab*-plane in this state. Consequently, the COO state shows up brightly in polarizing microscope images at the crossed-Nicols configuration [3]. Figures 2 show polarizing microscope images on the cleaved *ab*-plane of $La_{1/2}Sr_{3/2}MnO_4$ at 200 K. Corresponding to the field-induced melting of the COO, bright domains in zero field (Fig. 2(a)) become dark in 28 T (Fig. 2(b)).

The utilized camera has 12-bit resolution for intensity in each pixel, so that we can quantitatively analyze the obtained images in pulsed-fields. In Fig. 3, we show the intensity in a part of the images as a function of applied field at several temperatures. These clear changes in the optical intensity manifest the field-induced melting of the COO in contrast to rather moderate changes in magnetization and magneto-resistance in this temperature region [4]. The present result provides a novel opportunity for investigation of some kinds of field-induced transitions even in tiny crystals.

References

[1] Y. H. Matsuda *et al*., Physica B **346-347**, 519 (2004).
[2] Y. Narumi *et al*., J. Synchrotron Radiat. **13**, 271 (2006).
[3] T. Ogasawara *et al*., Phys. Rev. B **63**, 113105 (2001).
[4] M. Tokunaga *et al*., Phys. Rev. B **59**, 11151 (1999).

Authors

M. Tokunaga, I. Katakura, A. Matsuo, K. Kawaguchi, and K. Kindo